Alma Mater Studiorum · University of Bologna

School of Science
Department of Physics and Astronomy
Master Degree in Physics

Diffusion Model of the Hollow Electron Lens for HL-LHC

Supervisor:
Prof. Armando Bazzani

Co-supervisor:
Prof. Massimo Giovannozzi

Submitted by:
Giovanni Campri

Academic Year 2020/2021

è il mio vero nome . . .

Abstract

In the upcoming years, various upgrades and improvements are planned for the CERN Large Hadron Collider (LHC) and represent the mandate of the High-Luminosity project. The upgrade will allow for a total stored beam energy of about 700 MJ, which will need, among others, an extremely efficient collimation system. This will be achieved with the addition of a hollow electron lens (HEL) system to help control the beam-halo depletion and mitigate the effects of fast beam losses. In this master thesis, we present a diffusion model of the HEL for HL-LHC. In particular, we explore several scenarios to use such a device, focusing on the halo depletion efficiency given by different noise regimes.

Introduction

In the upcoming years, various upgrades and improvements are planned for the CERN Large Hadron Collider (LHC) and represent the mandate of the High-Luminosity project [1]. The upgrade, that will be implemented during the long shutdown in 2026-2028, will allow for an unprecedented total stored beam energy of about 700 MJ, which will need, among others, an extremely efficient collimation system, to avoid damage to ring components. Indeed, among the various improvements, an Hollow Electron Lens (HEL) system will be installed to help to control the beam-halo depletion and mitigate the effects of fast beam losses. The hollow beam of electrons generated by HEL is supposed to act on the beam by cleaning the tails while, ideally, leaving the beam core unperturbed. This kind of device has already been tested at the Fermilab Tevatron [2], where it turned out to be an effective tool to mitigate effects related to transient beam losses.

Various studies have been carried out recently [3, 4], simulating the effects of HEL on the beam-halo, and probing various working regimes of the electron beam. Among these, few random regimes are considered, thus, adding an element of stochasticity to the phenomenon. This opens the possibility to provide a description of the time evolution of the system, based on a diffusive framework, whose result is a Fokker-Planck approximation of the beam shape evolution [5].

In the work presented here, we introduce a simplified model of the HEL that represents its effect on the dynamics of the proton beam, and we prove the viability of a diffusive approach to describe the time evolution of the beam-halo. More in detail, we model the halo-depletion phenomenon as a diffusive process, starting from a stochastic symplectic map, and we make use of this model to probe various

working conditions, with the goal of finding the most efficient one in terms of fast beam-halo cleaning. We make use of 2D tracking simulations for the HEL system to make comparisons with the solutions of a Fokker-Planck equation, computed by means of a 2D Crank-Nicolson integrator [6]. In particular, we focus our study on the effects of different types of noise, represented by the electron beam working regimes, simulating many scenarios, and we show that the simulations results are expected and well explained by the diffusion model introduced.

Contents

List of Figures

List of Tables

Chapter 1

Review of Transverse Beam Dynamics

In this chapter we review the transverse beam dynamics in a synchrotron, introducing the basic concepts of the theory that describes betatron motion, which is a fundamental aspect of the study of accelerators physics.

1.1 Hamiltonian in Frenet-Serret coordinate system

The motion of charged particles in a circular accelerator is controlled by electric and magnetic fields that generate forces expressed by the general form of the Lorentz force [7]

$$\frac{d\mathbf{p}}{dt} = \mathbf{F} = e(\mathbf{E} + \mathbf{v} \times \mathbf{B}), \tag{1.1}$$

and the Hamiltonian for particle motion is

$$H = c\sqrt{m^2c^2 + (\mathbf{P} - e\mathbf{A})^2} + e\Phi, \tag{1.2}$$

where $\mathbf{A}$ and Φ are the vector and scalar potential, respectively, which are related to the electric and magnetic fields by

$$\mathbf{E} = -\nabla\Phi - \frac{\partial \mathbf{A}}{\partial t} \qquad \mathbf{B} = \nabla \times \mathbf{A}. \tag{1.3}$$

$\mathbf{P} = \mathbf{p} + e\mathbf{A}$ is the canonical and $\mathbf{p}$ is the mechanical momentum, and Hamilton's equations of motion read

$$\dot{x} = \frac{\partial H}{\partial P_x} \qquad \dot{P}_x = -\frac{\partial H}{\partial x} \qquad \text{etc.}, \tag{1.4}$$

where the dot represents the derivative with respect to time t and (x, P_x) are pairs of conjugate phase-space coordinates.

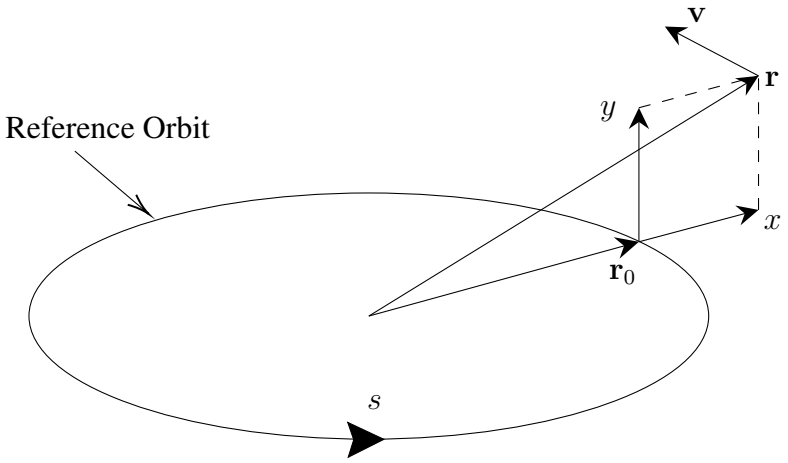

Figure 1.1: Curvilinear coordinate system for particle motion in a synchrotron. $\mathbf{r}_0(s)$ is the reference orbit, $\hat{x}$, $\hat{y}$ and $\hat{s}$ are the unit vectors describing the curvilinear coordinate system.

It is convenient to choose an appropriate new set of coordinates to describe the two components of the particle's motion in a circular accelerator, i.e. transverse and longitudinal motion.

Let $\mathbf{r}_0(s)$ be the reference orbit (see Fig. 1.1), where s is the arc length of the closed orbit measured from an initial point. The unit vector tangent to the closed orbit is

$$\hat{s}(s) = \frac{d\mathbf{r}_0}{ds}, \tag{1.5}$$

the unit vector on the tangential plane and perpendicular to the tangent vector is

$$\hat{x}(s) = -\rho(s)\frac{d\hat{s}(s)}{ds}, \tag{1.6}$$

where $\rho(s)$ is the curvature radius. The unit vector orthogonal to the tangential plane is given by

$$\hat{y}(s) = \hat{x}(s) \times \hat{s}(s). \tag{1.7}$$

The vectors $\hat{x}$, $\hat{s}$ and $\hat{y}$ form the orthonormal basis for the the right-handed Frenet-Serret curvilinear coordinate system with

$$\hat{x}'(s) = \frac{1}{\rho(s)}\hat{s}(s) + \tau(s)\hat{y}(s), \qquad \hat{y}'(s) = -\tau(s)\hat{x}(s), \tag{1.8}$$

where the prime denotes the differentiation with respect to s and $\tau(s)$ is the torsion of the curve which, discussing only the plane geometry, can be neglected. The particle trajectory around the reference orbit can be expressed as

$$\mathbf{r}(s) = \mathbf{r}_0(s) + x\hat{x}(s) + y\hat{y}(s). \tag{1.9}$$

In order to express the equations of motion in terms of the reference orbit coordinate system (x, s, y) we have to perform a canonical transformation by using the generating function

$$F_3(\mathbf{P}; x, s, z) = -\mathbf{P} \cdot [\mathbf{r}_0(s) + x\hat{x}(s) + y\hat{y}(s)], \tag{1.10}$$

where $\mathbf{P}$ is the particle's momentum in the Cartesian coordinate system, and the conjugate momenta for the coordinate (x, s, y) are given by

$$\begin{aligned} p_s &= -\frac{\partial F_3}{\partial s} = (1 + x/\rho)\mathbf{P} \cdot \hat{s}, \\ p_x &= -\frac{\partial F_3}{\partial x} = \mathbf{P} \cdot \hat{x}, \\ p_y &= -\frac{\partial F_3}{\partial y} = \mathbf{P} \cdot \hat{y}. \end{aligned} \tag{1.11}$$

Thus the new Hamiltonian becomes

$$H = e\phi + c\left\{m^2c^2 + \frac{(p_c - eA_s)^2}{(1+x/\rho)^2} + (p_x - eA_s)^2 + (p_y - eA_y)^2\right\}^{1/2}, \qquad (1.12)$$

where A_s, A_x and A_y are obtained by substitution of the vector $\mathbf{A}$ in Eq.(1.11)

$$A_s = (1+x/\rho)\mathbf{A}\cdot\hat{s}, \qquad A_x = \mathbf{A}\cdot\hat{x}, \qquad A_y = \mathbf{A}\cdot\hat{y}. \qquad (1.13)$$

We now want to use s as independent variable instead of time t. Using the relation $dH = (\partial H/\partial p_x)dp_x + (\partial H/\partial p_s)dp_s = 0$ or

$$x' = \frac{dx}{ds} = \frac{\dot{x}}{\dot{s}} = \left(\frac{\partial H}{\partial p_x}\right)\left(\frac{\partial H}{\partial p_c}\right)^{-1}, \qquad \text{etc.}, \qquad (1.14)$$

we find

$$\begin{aligned} t' &= \frac{\partial p_s}{\partial H}, & H' &= -\frac{\partial p_s}{\partial t} \\ x' &= -\frac{\partial p_s}{\partial p_x}, & p_x' &= \frac{\partial p_s}{\partial x} \\ y' &= -\frac{\partial p_s}{\partial p_y}, & p_y' &= \frac{\partial p_s}{\partial y} \end{aligned} \qquad (1.15)$$

where the prime denotes the differentiation with respect to s. The new Hamilton's equations are expressed with s as the independent variable, $-p_s$ as the new Hamiltonian, thus the conjugate phase-space coordinates are

$$(x, p_x) \qquad (y, p_y) \qquad (t, -H)\,. \qquad (1.16)$$

When the scalar and vector potentials ϕ and $\mathbf{A}$ are time independent, the new Hamiltonian $-p_s$ is also time independent and we are left with only two degrees of freedom. However, the new Hamiltonian depends on the variable s and, thanks to the nature of the circular accelerator, such dependence is periodic. The periodic nature of the new Hamiltonian can be exploited in the analysis of linear and non-linear betatron motion. The new Hamiltonian $\tilde{H} = -p_s$ is then given by

$$\tilde{H} = -\left(1+\frac{x}{\rho}\right)\left[\frac{(H-e\phi)^2}{c^2} - m^2c^2 - (p_x - eA_x)^2 - (p_y - eA_y^2))\right]^{1/2} - eA_s. \qquad (1.17)$$

The total energy and momentum of the particle are $E = H - e\phi$ and $p = \sqrt{E^2/c^2 - m^2c^2}$, respectively. We can expand the Hamiltonian up to second order in p_x and p_y since those are much smaller than the total momentum

$$\tilde{H} \approx -p\left(1 + \frac{x}{\rho}\right) + \frac{1 + x/\rho}{2p}\left[(p_x - eA_x)^2 + (p_y - eA_y)^2\right] - eA_s. \tag{1.18}$$

1.2 Magnetic field in Frenet-Serret coordinate system

In Frenet-Serret coordinate system, we have

$$\begin{aligned}
\nabla\Phi &= \frac{\partial\Phi}{\partial x}\hat{x} + \frac{1}{h_s}\frac{\partial\Phi}{\partial s}\hat{s} + \frac{\partial\Phi}{\partial y}\hat{y} \\
\nabla\cdot\mathbf{A} &= \frac{1}{h_s}\left[\frac{\partial(h_sA_1)}{\partial x} + \frac{\partial A_2}{\partial s} + \frac{\partial(h_sA_3)}{\partial y}\right] \\
\nabla\times\mathbf{A} &= \frac{1}{h_s}\left[\frac{\partial A_3}{\partial s} - \frac{\partial(h_sA_2)}{\partial y}\right]\hat{x} + \left[\frac{\partial A_1}{\partial y} - \frac{\partial A_3}{\partial x}\right]\hat{s} + \frac{1}{h_s}\left[\frac{\partial(h_sA_2)}{x} - \frac{\partial A_1}{\partial s}\right]\hat{y} \\
\nabla^2\Phi &= \frac{1}{h_s}\left[\frac{\partial}{\partial x}h_s\frac{\partial\Phi}{\partial x} + \frac{\partial}{\partial s}\frac{1}{h_s}\frac{\partial\Phi}{\partial s} + \frac{\partial}{\partial y}h_s\frac{\partial\Phi}{\partial y}\right],
\end{aligned} \tag{1.19}$$

where $h_s = 1 + x/\rho$, $A_1 = \mathbf{A}\cdot\hat{x}$, $A_2 = \mathbf{A}\cdot\hat{s} = A_s/h_s$ and $A_3 = \mathbf{A}\cdot\hat{y}$. In accelerator physics, we consider only the case with zero electric potential $\Phi = 0$, furthermore, for an accelerator with transverse magnetic fields, we assume $A_x = A_y = 0$. Thus, the two-dimensional magnetic field can be expressed as

$$\mathbf{B} = B_x(x,y)\hat{x} + B_y(x,y)\hat{y}, \tag{1.20}$$

where

$$B_x = -\frac{1}{h_s}\frac{\partial(h_sA_2)}{\partial y} = -\frac{1}{h_s}\frac{\partial A_s}{\partial y}, \qquad B_y = \frac{1}{h_s}\frac{\partial(h_sA_2)}{\partial x} = \frac{1}{h_s}\frac{\partial A_s}{\partial x}. \tag{1.21}$$

Using Maxwell's equation $\nabla\times\mathbf{B} = 0$, we get

$$\frac{\partial}{\partial y}\frac{1}{h_s}\frac{\partial A_s}{\partial y} + \frac{\partial}{\partial x}\frac{1}{h_s}\frac{\partial A_s}{\partial x} = 0. \tag{1.22}$$

For straight geometry with $h_s = 1$ we have $\nabla_\perp^2 A_s = 0$ and we can expand A_s in power series as

$$A_s = B_0 \mathbf{Re}\left[\sum_{n=0}^{\infty} \frac{b_n + ia_n}{n+1}(x+iy)^{n+1}\right], \tag{1.23}$$

where $B_x = -\frac{\partial A_s}{\partial y}$ and $B_y = \frac{\partial A_s}{\partial x}$. B_0 denotes the constant magnetic field provided by dipoles to keep a particle with momentum p_0 on an orbit with radius ρ_0, according to the relation

$$\frac{p_0}{e} = B_0 \rho_0, \tag{1.24}$$

where the r.h.s is the *magnetic rigidity*. The resulting magnetic flux density is given by the Beth representation

$$B_y + iB_x = B_0 \sum_{n=0}^{\infty} (b_n + ia_n)(x+iy)^n, \tag{1.25}$$

where

$$b_n = \frac{1}{B_0 n!}\frac{\partial^n B_y}{\partial x^n}\bigg|_{x=y=0} \qquad a_n = \frac{1}{B_0 n!}\frac{\partial^n B_x}{\partial x^n}\bigg|_{x=y=0}; \tag{1.26}$$

here b_n and a_n are the $2(n+1)$th multiple coefficients with dipole b_0 ($b_0 = 1$), dipole roll a_0, quadrupole b_1, skew quadrupole a_1, sextupole b_2, skew sextupole a_2 etc. The effective multipole field acting on the beam becomes

$$\frac{1}{B\rho}(B_y + iB_x) = \mp\frac{1}{\rho}\sum_{n=0}^{\infty}(b_n + ia_n)(x+iy)^n, \tag{1.27}$$

where $-$ and $+$ signs are for particles with positive and negative charges, respectively.

1.3 Betatron motion

If we ignore the effect of synchrotron motion, Hamilton's equations of motion are

$$x' = \frac{\partial \tilde{H}}{\partial p_x}, \qquad p_x' = -\frac{\partial \tilde{H}}{\partial x}, \qquad y' = \frac{\partial \tilde{H}}{\partial p_y}, \qquad p_y' = -\frac{\partial \tilde{H}}{\partial y}. \tag{1.28}$$

Considering the transverse magnetic field of Eq.(1.21), the equations describing the betatron motion are given by

$$\begin{cases} x'' - \dfrac{\rho + x}{\rho^2} = \pm \dfrac{B_y}{B\rho} \dfrac{p_0}{p} \left(1 + \dfrac{x}{\rho}\right)^2 \\ y'' = \mp \dfrac{B_x}{B\rho} \dfrac{p_0}{p} \left(1 + \dfrac{x}{\rho}\right)^2 \end{cases} \tag{1.29}$$

where higher-order terms are neglected, the upper and lower signs correspond to the positive and negative charges, respectively, p is the momentum of the particle, p_0 is the momentum of a reference particle.

Considering an on-momentum particle ($p = p_0$) and expanding the magnetic field up to the first order, we get

$$B_y = -B_0 + \frac{\partial B_y}{\partial x} x = \mp B_0 + B_1 x, \qquad B_x = \frac{\partial B_y}{\partial x} y = B_1 y, \tag{1.30}$$

where the quadrupole gradient function $B_1 = \partial B_y / \partial x$ is evaluated at the closed orbit defined by the dipole field. The equations of the betatron motion then become

$$\begin{cases} x'' + K_x(s) x = 0 & K_x = 1/\rho^2 \mp K_1(s) \\ y'' + K_y(s) y = 0 & K_y = \pm K_1(s) \end{cases} \tag{1.31}$$

where $K_1(s) = B_1(s)/B\rho$ is the effective focusing function. Eqs.(1.31) are called Hill's equations and have the structure of a linear oscillator with s-dependent frequency.

1.4 Linear transfer maps

1.4.1 Element maps

Since the gradients are constant throughout a single magnet, we can introduce the transfer map $\mathbf{M}^{(l)}$ of the magnetic element $\mathcal{M}^{(l)}$ (see Fig.1.2). We define $\mathbf{M}^{(l)}$ as the function that transforms the phase-space coordinates $\mathbf{x}(s_{l-1})$ to $\mathbf{x}(s_l)$ [8]

$$\mathbf{x}(s_l) = \mathbf{M}^{(l)}(\mathbf{x}(s_{l-1})) \qquad \mathbf{M}^{(l)} : \mathbb{R}^4 \longrightarrow \mathbb{R}^4, \tag{1.32}$$

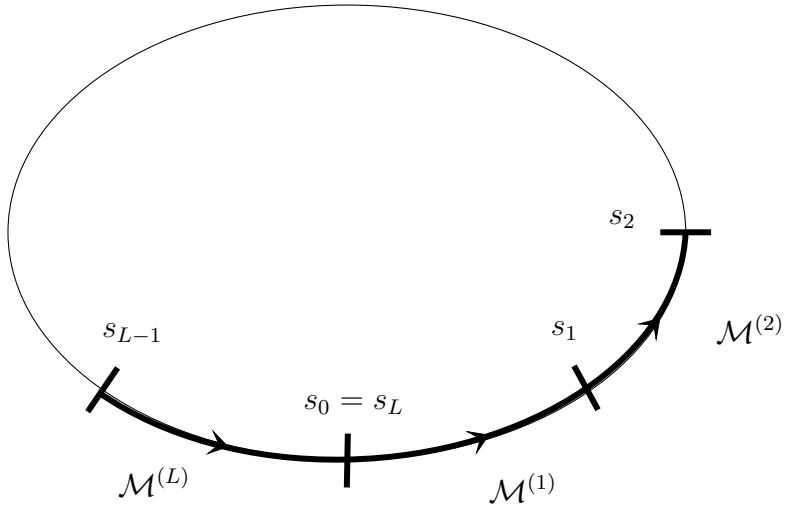

Figure 1.2: Sketch of the magnetic elements along a circular accelerator

where in its component $\mathbf{M}^{(l)}$ is given by

$$\begin{aligned} x(s_l) &= x_1(s_l) = M_1^{(l)}(\mathbf{x}(s_{l-1})) \\ p_x(s_l) &= x_2(s_l) = M_2^{(l)}(\mathbf{x}(s_{l-1})) \qquad M_j^{(l)} : \mathbb{R}^4 \longrightarrow \mathbb{R} \qquad j = 1,2,3,4; \\ y(s_l) &= x_3(s_l) = M_3^{(l)}(\mathbf{x}(s_{l-1})) \\ p_y(s_l) &= x_4(s_l) = M_4^{(l)}(\mathbf{x}(s_{l-1})) \end{aligned} \tag{1.33}$$

here we are introducing this new coordinates notation for the sake of simplicity. We denote $s_0 = 0$, thus s_L represents the total length of the accelerator. The transfer map $\mathbf{M}^{(l)}$ can be seen as the Hamiltonian flow that propagates the initial condition $\mathbf{x}(s_{l-1})$ to $\mathbf{x}(s_l)$.

A map $\mathbf{M} : \mathbb{R}^4 \longrightarrow \mathbb{R}^4$ is symplectic if its Jacobian $\mathbf{M}_J$ is a symplectic matrix for every $\mathbf{x}$, which means that it satisfies

$$\mathbf{M}_J(\mathbf{x})\mathbf{J}\mathbf{M}_J^T(\mathbf{x}) = \mathbf{J}, \tag{1.34}$$

where $\mathbf{M}_J^T$ denotes the transposed matrix and $\mathbf{J}$ is defined as

$$\mathbf{J} = \begin{pmatrix} 0 & 1 & 0 & 0 \\ -1 & 0 & 0 & 0 \\ 0 & 0 & 0 & 1 \\ 0 & 0 & -1 & 0 \end{pmatrix}. \tag{1.35}$$

An equivalent definition of symplectic map can be given in terms of Poisson brackets. Given two function $f, g : \mathbb{R}^4 \longrightarrow \mathbb{R}$ defined on the phase space, the Poisson bracket of f, g is defined by

$$\{f, g\} = \sum_{i=x,y} \frac{\partial f}{\partial x_i}\frac{\partial g}{\partial p_i} - \frac{\partial f}{\partial p_i}\frac{\partial g}{\partial x_i}. \tag{1.36}$$

Therefore $\mathbf{M}$ is symplectic if

$$\{M_i, M_j\} = \mathbf{J}_{i,j} \qquad i, j = 1, ..., 4. \tag{1.37}$$

Furthermore, we define a map $\mathbf{M} : \mathbb{R}^2 \longrightarrow \mathbb{R}^2$ area-preserving, if its Jacobian has a determinant equal to one:

$$\mathbf{Det}(\mathbf{M}_J) \equiv \frac{\partial M_1}{\partial x}\frac{\partial M_2}{\partial p} - \frac{\partial M_1}{\partial p}\frac{\partial M_2}{\partial x} = 1, \tag{1.38}$$

which is actually equivalent to the symplectic condition in $\mathbb{R}^2$, thus the symplectic condition can be seen as the generalization of the area-preserving condition to higher dimensionality.

1.4.2 The one-turn map

The one-turn map is a Poincaré map at section $s = s_0$ given by the composition of the maps of the single elements of the accelerator:

$$\mathbf{M} = \mathbf{M}^{(L)} \circ \mathbf{M}^{(L-1)} \circ ... \circ \mathbf{M}^{(2)} \circ \mathbf{M}^{(1)}. \tag{1.39}$$

$\mathbf{M}$ transforms the phase space coordinate $\mathbf{x}(s_0)$ in to $\mathbf{x}(s_L)$ after one full turn around the accelerator

$$\mathbf{x}(s_L) = \mathbf{M}(\mathbf{x}(s_0)). \tag{1.40}$$

Separating the linear from the non linear contribution, we can express $\mathbf{M}$ as

$$\mathbf{M}(\mathbf{x}) = \mathbf{L}(\mathbf{x}) + O(|\mathbf{x}|^2), \tag{1.41}$$

where $\mathbf{L}$ is the linearized map whose action on the coordinate is

$$x_j(s_L) = \sum_{k=1}^{4} \mathbf{L}_{j,k} x_k(s_0). \tag{1.42}$$

We can classify the one-turn linear transfer map $\mathbf{L}$, or a generic symplectic 2×2 matrix, according to the nature of its eigenvalues λ_1, λ_2. The area preserving condition imposes that $\lambda_1 \cdot \lambda_2 = 1$. Since the matrix is real, we have the following cases:

$$|\mathbf{Tr}(\mathbf{L})| \begin{cases} < 2 & \lambda_1 = \lambda_2^* = e^{i\omega} \qquad \omega \in \mathbb{R} \qquad \text{elliptic} \\ = 2 & \lambda_1 = \lambda_2 = \pm 1 \qquad\qquad\qquad \text{parabolic} \\ > 2 & \lambda_2 = 1/\lambda_1 = \pm e^{\tau} \qquad \tau \in \mathbb{R} \qquad \text{hyperbolic} \end{cases} \tag{1.43}$$

where λ^* denotes the complex conjugate of λ. Therefore, a necessary condition for the orbit stability is

$$|\mathbf{Tr}(\mathbf{L})| \leq 2. \tag{1.44}$$

1.4.3 Linear transfer maps of magnetic elements

We can now express the map of the main three elements of an accelerator: drift space, dipole magnet, and quadrupole magnet. A drift space is a field free region, where the particle drifts without any change of momentum. The corresponding linear map is given by

$$\mathbf{L}_{drift} = \begin{pmatrix} 1 & \ell & 0 & 0 \\ 0 & 1 & 0 & 0 \\ 0 & 0 & 1 & \ell \\ 0 & 0 & 0 & 1 \end{pmatrix}, \tag{1.45}$$

where ℓ is the length of the element.

The dipole magnet is an element whose purpose is to bend the beam around the accelerator lattice. It is a straight section of length ℓ with constant dipolar filed B_0, $K_1 = 0$ and its map is given by

$$\mathbf{L}_{dipole} = \begin{pmatrix} 1 & \rho \sin\frac{\ell}{\rho} & 0 & 0 \\ 0 & 1 & 0 & 0 \\ 0 & 0 & \cos\frac{\ell}{\rho} & \rho \sin\frac{\ell}{\rho} \\ 0 & 0 & -\rho^{-1}\sin\frac{\ell}{\rho} & \cos\frac{\ell}{\rho} \end{pmatrix}, \tag{1.46}$$

which correspond to a rectangular magnet and takes in consideration the edge focusing effect.

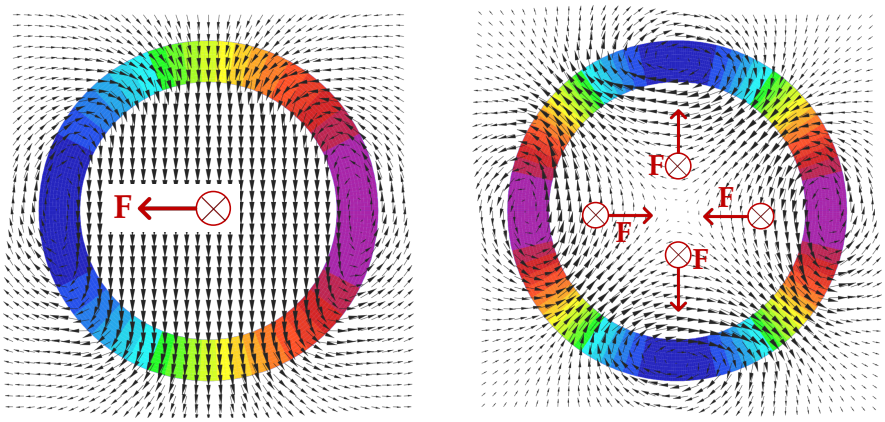

Figure 1.3: Ideal dipole (left), and ideal focusing quadrupole (right). The black arrows represent the magnetic field, the current in the coils are indicated in colour and the particles are directed toward the page [9].

The quadrupole is a section that has the function to focusing or defocusing the beam; when focusing in one plane, it defocuses in the other one. Usually, we refer to a focusing quadrupole when it focuses in the horizontal plane as seen in Fig.1.3, and to a defocusing quadrupole when it focuses in the vertical plane.

A quadrupole is characterised by $\rho = \infty$, $K_1 > 0$, and the linear map is given by

$$\mathbf{L}_{quad} = \begin{pmatrix} \cos\left(\sqrt{K_1}\ell\right) & \frac{1}{\sqrt{K_1}}\sin\left(\sqrt{K_1}\ell\right) & 0 & 0 \\ -\sqrt{K_1}\sin\left(\sqrt{K_1}\ell\right) & \cos\left(\sqrt{K_1}\ell\right) & 0 & 0 \\ 0 & 0 & \cosh\left(\sqrt{K_1}\ell\right) & \frac{1}{\sqrt{K_1}}\sinh\left(\sqrt{K_1}\ell\right) \\ 0 & 0 & \sqrt{K_1}\sinh\left(\sqrt{K_1}\ell\right) & \cosh\left(\sqrt{K_1}\ell\right) \end{pmatrix}, \tag{1.47}$$

where we are representing the map for the horizontal focusing quadrupole, while the one for the defocusing quadrupole is given by the same expression where the two diagonal blocks are interchanged.

1.5 Solution of Hill's equations

It is possible to write down the solution to the Hill's equation (Eqs.(1.31)) using the ansatz

$$\begin{cases} x(s) = \sqrt{2J_x\beta_x(s)}\sin(\phi_x(s) + \delta_x) \\ y(s) = \sqrt{2J_y\beta_y(s)}\sin(\phi_y(s) + \delta_y) \end{cases} \tag{1.48}$$

where β_x and β_y are function of s defining the amplitudes of the oscillations, ϕ_x and ϕ_y are phase advances while δ_x, δ_y, J_x and J_y are constants related to the initial conditions.

Substituting the ansatz in the Hill's equations we find

$$\begin{aligned} &\phi'_x\beta'_x + \phi''_x\beta_x = 0 \\ &\phi'_y\beta'_y + \phi''_y\beta_y = 0 \\ &\beta''_x\frac{1}{2} - \beta'^2_x\frac{1}{4\beta_x} - \beta_x\phi'^2_x + \beta_x K_x = 0 \\ &\beta''_y\frac{1}{2} - \beta'^2_y\frac{1}{4\beta_y} - \beta_y\phi'^2_y + \beta_y K_y = 0, \end{aligned} \tag{1.49}$$

where from the first two equations we find the relation between the amplitude and phase advance

$$\phi_x(s) = c_x\int_0^s \frac{d\sigma}{\beta_x(\sigma)} \qquad \phi_y(s) = c_y\int_0^s \frac{d\sigma}{\beta_y(\sigma)} \tag{1.50}$$

where c_x and c_y are constant and the calculation is set so that $\phi_x(0) = \phi_y(0) = 0$. β_x and β_y are called betatron functions, and setting $c_x = c_y = 1$ we determine them uniquely.

The linear tunes of the machine are defined as

$$\nu_x = \frac{\phi_x(s_L)}{2\pi} \qquad \nu_y = \frac{\phi_y(s_L)}{2\pi} \tag{1.51}$$

often denoted as Q_x and Q_y, such definition holds for every order in the multipole expansion. Tunes have a central role in the design and control of the beam due to resonances. A resonance emerges when the tune and the frequency of a periodic perturbation have the same value. The resonant condition leads to beam

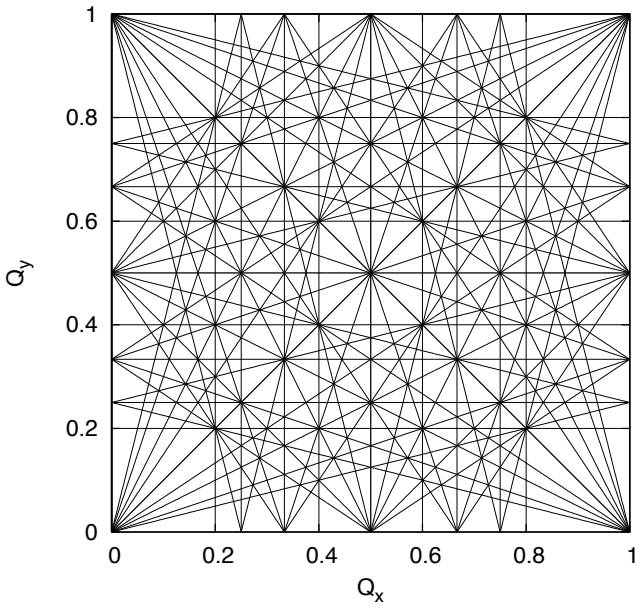

Figure 1.4: Working point diagram, representing resonances in tune space, for $k \leq 5$ [9].

deterioration, therefore one usually wants to maintain the system at a working point far from resonances, i.e. far from lines of a working diagram (see Fig. 1.4). The equation for resonant condition is given by

$$mQ_x + nQ_y = p \qquad m, n, p \in \mathbb{Z}, \tag{1.52}$$

and the order of resonance is given by

$$k = |n| + |m|. \tag{1.53}$$

1.6 Courant-Snyder parametrisation

We now write down the expression for the one-turn linear map according to the above formalism, considering Eqs.(1.48) we write

$$\mathbf{x}(s_L) = \mathbf{L}_{Twiss}\mathbf{x}(s_0); \tag{1.54}$$

here $\mathbf{L}$ is the Twiss matrix

$$\mathbf{L}_{Twiss} = \begin{pmatrix} \mathbf{L}_x & 0 \\ 0 & \mathbf{L}_y \end{pmatrix}, \tag{1.55}$$

where

$$\mathbf{L}_x = \begin{pmatrix} \cos(2\pi\nu_x) + \alpha_x \sin(2\pi\nu_x) & \beta_x \sin(2\pi\nu_x) \\ -\gamma_x \sin(2\pi\nu_x) & \cos(2\pi\nu_x) - \alpha_x \sin(2\pi\nu_x) \end{pmatrix}, \tag{1.56}$$

and a similar expression holds for the matrix $\mathbf{L}_y$. Here α and γ are given by

$$\alpha = -\frac{\beta'}{2}, \qquad \gamma = \frac{1+\alpha^2}{\beta}. \tag{1.57}$$

α, β, γ are all functions of s, they are known as Twiss parameters and, in Eq.(1.56), they are evaluated at $s = 0$. Setting z as either the horizontal or vertical coordinate,

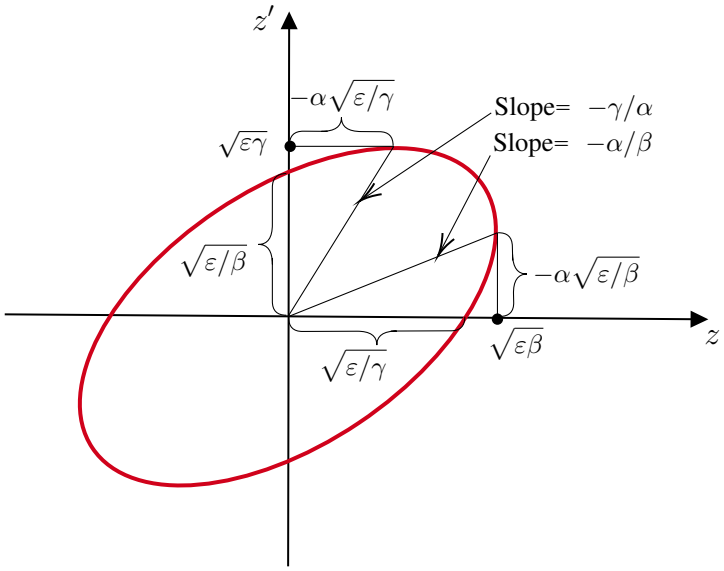

Figure 1.5: The Courant-Snyder invariant ellipse. α, β and γ are the Twiss parameters, while ε is the Courant-Snyder invariant, which gives the area of the ellipse.

the first integral of motion, or Courant-Snyder invariant, is given by

$$C(z, z') = \gamma_z z^2 + 2\alpha_z z z' + \beta_z z' = 2J_z \equiv \varepsilon_z. \tag{1.58}$$

The Twiss parameters define the Courant-Snyder ellipse in the (z, z') plane, and ε gives the area of such ellipse (see Fig. 1.5). Thus during the motion of the particle, the shape and slope of the ellipse may vary, but its area remains constant. It is however possible to deal with circles in the phase space instead of ellipses passing to the Courant-Snyder coordinates [10]. Indeed we can express $\mathbf{L}_{Twiss}$ as

$$\mathbf{L}_{Twiss} = \mathbf{T}\mathbf{R}\mathbf{T}^{-1} \tag{1.59}$$

where

$$\mathbf{R} = \begin{pmatrix} \cos\phi_x & \sin\phi_x & 0 & 0 \\ -\sin\phi_x & \cos\phi_x & 0 & 0 \\ 0 & 0 & \cos\phi_y & \sin\phi_y \\ 0 & 0 & -\sin\phi_y & \cos\phi_y \end{pmatrix}, \tag{1.60}$$

is a simple rotation matrix, and

$$\mathbf{T} = \begin{pmatrix} \sqrt{\beta_x} & 0 & 0 & 0 \\ \frac{-\alpha_x}{\sqrt{\beta_x}} & \frac{1}{\sqrt{\beta_x}} & 0 & 0 \\ 0 & 0 & \sqrt{\beta_y} & 0 \\ 0 & 0 & \frac{-\alpha_y}{\sqrt{\beta_y}} & \frac{1}{\sqrt{\beta_y}} \end{pmatrix}, \tag{1.61}$$

is the map that conjugates the coordinates $\mathbf{x}$ to the Courant-Snyder coordinates $\hat{\mathbf{x}}$. In these new coordinates, the motion is represented only by a simple rotation in the phase space, we have

$$\hat{\mathbf{x}} = \mathbf{T}^{-1}\mathbf{x} \qquad \hat{\mathbf{x}}(s_L) = \mathbf{R}\hat{\mathbf{x}}(s_0). \tag{1.62}$$

Such parametrization transforms the ellipse, in the phase space, into a circle, as seen in Fig. 1.6.

The invariant of the map is now expressed as

$$\varepsilon_z = \hat{z}^2 + \hat{p_z}^2 = 2J_z, \tag{1.63}$$

being J the action of the particle, we see that the invariant is two times the action variable. It is to be noted that when the particles accelerate they undergo the so-called adiabatic damping, which decreases the area of the ellipse with the

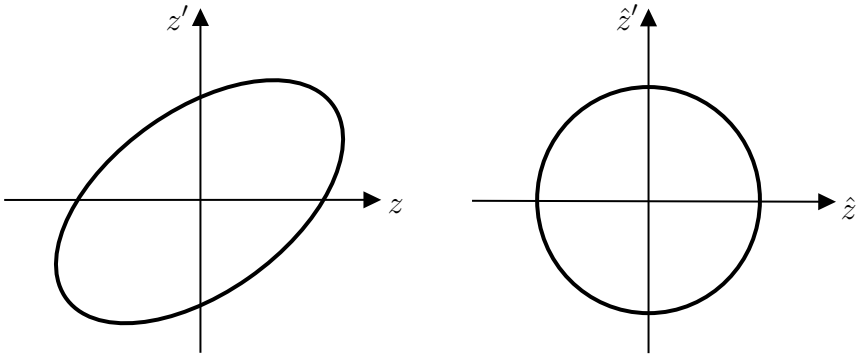

Figure 1.6: Representation of the phase space in the physical coordinates (left), and in the Courant-Snyder coordinates (right). The change of coordinates transforms the ellipse into a circle.

increasing of the energy of the beam. We then define the normalised emittance, that is constant regardless of the energy of the particles, as

$$\varepsilon_z^* \equiv \beta_{rel}\gamma_{rel}\varepsilon_z, \tag{1.64}$$

where β_{rel} and γ_{rel} are the relativistic functions.

The Courant-Snyder invariant is a property of the single particle, while usually, inside a beam, we have a distributions of many particles. Such distribution, usually Gaussian, can be described by a covariance matrix, namely the beam matrix, given by

$$\mathbf{\Sigma} = \begin{pmatrix} \sigma_z^2 & \sigma_{z,z'} \\ \sigma_{z,z'} & \sigma_{x'}^2 \end{pmatrix} \tag{1.65}$$

where, for a normalised distribution $\rho(z, z')$,

$$\begin{aligned} \langle z \rangle = \int z\rho(z,z')dz\,dz' \qquad \langle z' \rangle = \int z'\rho(z,z')dz\,dz' \\ \sigma_z^2 = \int (z - \langle z \rangle)^2 \rho(z,z')dz\,dz' \qquad \sigma_{z'}^2 = \int (z' - \langle z' \rangle)^2 \rho(z,z')dz\,dz' \\ \sigma_{zz'} = \int (z - \langle z \rangle)(z' - \langle z' \rangle)dz\,dz'. \end{aligned} \tag{1.66}$$

From the determinant of the beam matrix, we define the geometric emittance, or rms emittance

$$\varepsilon_{rms} = \sqrt{\mathbf{Det}(\mathbf{\Sigma})} = \sqrt{\sigma_z^2\sigma_{z'}^2 - \sigma_{zz'}^2} = \mathcal{A}/\pi \tag{1.67}$$

where $\mathcal{A}$ is the area of the distribution in the phase space.

1.7 Non-linear transfer maps

Up until now, we only considered the motion of particles in the linear case. In the general case, the transfer map of a non linear element $\mathcal{M}^{(l)}$, like a sextupole or an higher order multipole, cannot be computed exactly. The Hill's equations in the non-linear case, neglecting the linear coupling, are given by

$$\begin{cases} x'' + K_x(s)x = \mathbf{Re}\left[\sum_{n=0}^{\infty} \frac{(b_n + ia_n)}{n!}(x+iy)^n\right] \\ \\ y'' + K_y(s)y = -\mathbf{Im}\left[\sum_{n=0}^{\infty} \frac{(b_n + ia_n)}{n!}(x+iy)^n\right] , \end{cases} \tag{1.68}$$

which can be rewritten as a first order differential equation for $\mathbf{x} = (x, p_x, y, p_y)$

$$\frac{d\mathbf{x}}{ds} = \mathbf{A}(s)\mathbf{x} + \mathbf{f}(x, y; s), \tag{1.69}$$

where $\mathbf{A}$ and $\mathbf{f}$ are the linear and non-linear contributions respectively.

We now define $\mathbf{L}(s, s_{l-1})$ as the fundamental matrix for the linear system satisfying the equation

$$\frac{d\mathbf{L}(s, s_{l-1})}{ds} = \mathbf{A}(s)\mathbf{L}(s, s_{l-1}) \qquad \mathbf{L}(s_{l-1}, s_{l-1}) = \mathbf{I}, \tag{1.70}$$

with the semigroup property

$$\mathbf{L}(s_{\prime\prime}, s_{\prime})\mathbf{L}(s_{\prime}, s) = \mathbf{L}(s_{\prime\prime}, s). \tag{1.71}$$

The non-linear equation 1.69 can now be written in the integral form

$$\begin{aligned} \mathbf{x}(s) &= \mathbf{L}(s, s_{l-1})\mathbf{x}(s_{l-1}) + \int_{s_{l-1}}^{s} \mathbf{L}(s, s_{\prime})\mathbf{f}(x, y; s_{\prime})ds_{\prime} \\ &= \mathbf{L}(s, s_{l-1})\left(\mathbf{x}(s_{l-1}) + \int_{s_{l-1}}^{s} \mathbf{L}(s_{l-1}, s_{\prime})\mathbf{f}(x, y; s_{\prime})ds_{\prime}\right), \end{aligned} \tag{1.72}$$

where $\mathbf{x}(s_{l-1})$ is the initial condition.

1.7.1 Thin lens approximation

The thin lens approximation allow us to approximate the element map $\mathcal{M}^{(l)}$ to a polynomial form, by making the assumption that non linearity is concentrated in one or more points of the interval $[s_{l-1}, s_l]$. Such approach has the advantage to provide a map that is symplectic and easy to implement on a tracking code.

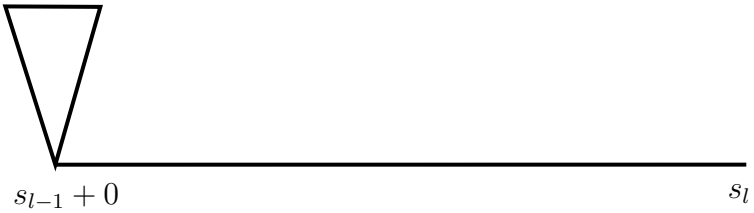

Figure 1.7: Sketch of the one-kick approximation.

The one-kick approximation consists in solving Eq. (1.72) by considering the non-linear contribution $\mathbf{f}$ acting only in the initial part of the element (see Fig.1.7). Thus we make the substitution

$$\mathbf{f}(x, y; s) \longrightarrow \mathbf{f}(x, y; s)\ell\delta(s - (s_{l-1} + 0)) \tag{1.73}$$

where δ is the delta function defined according to

$$\int_{0-\epsilon}^{0+\epsilon} \delta(s)ds = 1 \qquad \int_{0-\epsilon}^{0+\epsilon} \delta(s)\mathbf{f}(x, y; s)ds = \mathbf{f}(x, y; 0) \qquad \forall\epsilon \in \mathbf{R}^+. \tag{1.74}$$

In Eq. (1.73), we write plus zero because the nonlinearity acts only at the beginning of the element. From $s_{l-1} + \epsilon$ to s_l the nonlinearity is absent, thus, making the computation of the transfer map we have

$$\mathbf{x}(s_l) = \mathbf{L}(s_l, s_{l-1} + \epsilon)\mathbf{x}(s_{l-1} + \epsilon). \tag{1.75}$$

The non-linear kick has no effect on the coordinate x

$$\int_{s_{l-1}}^{s_{l-1}+\epsilon} \frac{dx}{ds}ds = x(s_{l-1} + \epsilon) - x(s_{l-1}) = \mathcal{O}(\epsilon), \tag{1.76}$$

while in the coordinate p_x there is a discontinuity

$$\int_{s_{l-1}}^{s_{l-1}+\epsilon} \frac{dp_x}{ds}ds = p_x(s_{l-1} + \epsilon) - p_x(s_{l-1}) = \ell f_x(x, y; s_{l-1}) + \mathcal{O}(\epsilon), \tag{1.77}$$

and the same can be written for y and p_y. In the limit $\epsilon \longrightarrow 0$ we find the kick map

$$\begin{pmatrix} x \\ p_x \\ y \\ p_y \end{pmatrix}_{s=s_{l-1}+0} = \begin{pmatrix} x \\ p_x + \ell f_x(x,y;s) \\ y \\ p_y + \ell f_y(x,y;s) \end{pmatrix}_{s=s_{l-1}} . \tag{1.78}$$

The one-kick approximation is then given by the composition of the linear and kick maps

$$\mathbf{x}_{one-kick}(s_l) = \mathbf{L}(s_l, s_{l-1})(\mathbf{x}(s_{l-1}) + \ell \mathbf{f}(x, y; s_{l-1})). \tag{1.79}$$

This approach can be taken forward if we split the element in m portions and apply to each of them the one-kick approximation. By increasing the number of portions of the element, we decrease the error of the symplectic map, which can be estimated to be $\mathcal{O}(\ell^2/m)$.

1.8 Dynamic Aperture

Beam stability is an important task in accelerators physics, which is made possible using various multipolar magnetic elements. It is not just a matter of keeping the beam inside the mechanical aperture of the machine, because the nonlinearities largely reduce the area of the phase space in which stable orbits are possible.

The dynamic aperture (DA) [11] is the amplitude of the phase space region in which stable motion occurs. Such quantity, is a key one for the design of modern colliders that rely on superconducting magnets having unavoidable non-linear field errors. Thus, defining and controlling the DA is crucial.

In theory, the motion stability definition requires a large time scale, however, in practice, we can consider a maximum number of turns N_{max} that is determined on the basis of the specific case. Let (x, y) be the transverse spatial coordinates describing the betatronic motion, if an ensemble of initial conditions defined on a polar grid

$$x = r\cos\theta, \qquad y = r\sin\theta, \qquad 0 \leq \theta \leq \pi/2, \tag{1.80}$$

where x, y are expressed in units σ_x, σ_y of the beam dimension is tracked for up to N_{max} turns, then a measure of the DA can be defined as

$$\mathcal{D}(N) = \frac{2}{\pi} \int_0^{\pi/2} r(\theta; N) d\theta, \tag{1.81}$$

where $r(\theta; N)$ is the last stable amplitude for up to N turns in the direction θ. Thus, DA can be considered a function of N, with an asymptotic value representing the DA for an arbitrary large time.

Chapter 2

Stochastic Hamiltonians and Diffusive Approach

Stochastic differential equations describe the evolution of systems subjected to deterministic interaction, in presence of fluctuating terms with known statistical properties. Such fluctuations are due to external factors which can undergo rapid and unpredictable variations, or due to the presence of other random interactions. The integrartion of stochastic differential equations is an essential tools to approach formulation of non-equilibrium Statistical Mechanics in complex systems physics, and requires new mathematical concepts (i.e. the Wiener process and the Ito integral [12, 13]). To use the evolution laws that could be applicable to real system, to describe and make a prediction about macroscopic observables, one need two hypotheses to be verified: the microscopic dynamics should have a strong dependence on the initial conditions, and the system should be decomposable into elementary almost-independent components. Once both of these hypotheses are verified, we can use stochastic differential equations as mathematical model for Statistical Mechanics of physical systems.

2.1 Stochastic Hamiltonian systems

We now consider a system whose dynamics can be described by a stochastically perturbed Hamitonian system. In the 1DoF case the Hamiltonian reads

$$H = H_0(I) + \xi(t)H_1(I,\theta), \tag{2.1}$$

where (I,θ) are action-angle variables, H_1 is a perturbation and $\xi(t)$ represents a random noise, with a correlation function given by

$$\langle \xi(t)\xi(t+T)\rangle = \sigma^2\phi(\gamma T) \qquad \phi(\gamma T) \simeq e^{-\gamma T}, \tag{2.2}$$

where γ^{-1} is the correlation time scale, that defines the noise evolution with respect to the characteristic time scale of the unperturbed dynamics H_0. In the white noise limit we have that

$$\sigma^2\phi(\gamma T) \longrightarrow \delta(T), \tag{2.3}$$

and without loss of generality, we can assume $\langle\xi\rangle = 0$.

Each orbit is a superposition of a regular dynamics, given by H_0, and the effects of fluctuations due to the stochastic perturbation. $H_1(I,\theta)$ describes the amplitude of the perturbation and we assume that $\|H_1\| \ll \|H_0\|$. We introduce a small parameter $\epsilon = \|H_1\| \ll 1$ to denote the L^2-norm of H_1, and we define $\hat{H}_1 = H_1/\|H_1\|$. In the limit of small perturbations, under suitable assumptions, it is possible to study the dynamics of the integral of motion as a diffusion process in a slow evolution time $\tau = \epsilon^2 t$, for which the white noise approximation is justified. The slow time defines the time scale for the diffusion of the action variable; while the angle variables can be considered as fast variables, which decorrelate in a time much shorter than the diffusion time scale.

Indeed we can establish a relation between the various time scales of the system:

- γ^{-1} is the noise decorrelation time scale and it is the shortest time scale. We require that, in a time γ^{-1} the action I can be considered constant;
- the phase relaxation time scale is given by [15]

$$T_\theta \simeq \epsilon^{-2/3} \left\| \frac{\partial \hat{H}_1}{\partial \theta} \right\|^{-2/3} \left\| \frac{\partial \Omega}{\partial I} \right\|^{-1}, \tag{2.4}$$

where $\Omega = \partial H_0/\partial I \neq 0$ is the phase advance;

- the action-diffusion time scale is the larger time scale and it is given by

$$T_I \simeq \epsilon^{-2} \left\| \frac{\partial \hat{H}_1}{\partial \theta} \right\|^{-2}, \tag{2.5}$$

  i.e. the scale at which the perturbation may change the average dynamics of the action variable by a quantity $\mathcal{O}(1)$.

Then if $\epsilon \ll 1$ we have that $\gamma^{-1} \ll T_\theta \ll T_I$.

To resume, we expect the angle variable to make a great number of turns with angular velocity Ω along an unperturbed orbit before the diffusion of the action variable becomes relevant. This fact means that we are justified to use an averaging principle that allow us to make an average on the angle variable, to describe the evolution of the system only by means of the action variable.

Under the previous assumptions, having the angle distribution relaxed to a uniform one, the action distribution $\rho(I, \tau)$ satisfies the Fokker-Planck (FP) equation, as we will derive in the next section, of the form

$$\frac{\partial \rho}{\partial \tau} = \frac{1}{2} \frac{\partial}{\partial I_i} D_{ij}(I) \frac{\partial \rho}{\partial I_j}, \tag{2.6}$$

with an action-dependent diffusion coefficient given by

$$D_{ij}(I) = \frac{1}{(2\pi)^d} \int_{\mathbb{T}^d} \left(\frac{\partial \hat{H}_1}{\partial \theta_i} \frac{\partial \hat{H}_1}{\partial \theta_j} \right) d\theta \qquad 1 \leq i, j \leq d. \tag{2.7}$$

2.2 Derivation of the diffusion equation

We are now going to derive the Fokker-Planck equation considering all assumptions made up to now. Starting from the one-dimensional Hamiltonian [16]

$$H = H_0(I) + \epsilon \xi(t) H_1(I, \theta) \tag{2.8}$$

where $\epsilon \longrightarrow 0$ and $\xi(t)$ is a stationary random process satisfying the white noise condition of Eq. (2.3), and with average $\langle \xi \rangle = 0$. We consider the evolution of

particle density $\rho(I,\theta,t)$ in phase space, described by a stochastic Liouville equation that reads

$$\frac{\partial\rho}{\partial t}+\Omega\frac{\partial\rho}{\partial\theta}+\epsilon\xi(t)\left(\frac{\partial H_1}{\partial I}\frac{\partial\rho}{\partial\theta}-\frac{\partial H_1}{\partial\theta}\frac{\partial\rho}{\partial I}\right)=0. \tag{2.9}$$

We separate the density average from its fluctuating part

$$\rho=\rho_0+\epsilon\rho_1,\qquad \rho_0=\langle\rho\rangle,\qquad \langle\rho_1\rangle=0. \tag{2.10}$$

Then, the equation reads

$$\begin{aligned}\frac{\partial\rho_0}{\partial t}+\Omega\frac{\partial\rho_0}{\partial\theta}+\epsilon\left(\frac{\partial\rho_1}{\partial t}+\Omega\frac{\partial\rho_1}{\partial\theta}\right)+\epsilon\xi(t)\left(\frac{\partial H_1}{\partial I}\frac{\partial\rho_0}{\partial\theta}-\frac{\partial H_1}{\partial\theta}\frac{\partial\rho_0}{\partial I}\right)\\ +\epsilon^2\xi(t)\left(\frac{\partial H_1}{\partial I}\frac{\partial\rho_1}{\partial\theta}-\frac{\partial H_1}{\partial\theta}\frac{\partial\rho_1}{\partial I}\right)=0.\end{aligned} \tag{2.11}$$

Making the average, we obtain

$$\frac{\partial\rho_0}{\partial t}+\Omega\frac{\partial\rho_0}{\partial\theta}+\epsilon^2\left\langle\xi(t)\left(\frac{\partial H_1}{\partial I}\frac{\partial\rho_1}{\partial\theta}-\frac{\partial H_1}{\partial\theta}\frac{\partial\rho_1}{\partial I}\right)\right\rangle=0. \tag{2.12}$$

Subtracting Eq. (2.12) from Eq. (2.11) we have

$$\frac{\partial\rho_1}{\partial t}+\Omega\frac{\partial\rho_1}{\partial\theta}=\xi(t)g(I,\theta,t)+\mathcal{O}(\epsilon), \tag{2.13}$$

where we have lightened the notation by setting

$$g(I,\theta,t)=-\left(\frac{\partial H_1}{\partial I}\frac{\partial\rho_0}{\partial\theta}-\frac{\partial H_1}{\partial\theta}\frac{\partial\rho_0}{\partial I}\right). \tag{2.14}$$

We now look for a solution for Eq. (2.13) with the initial condition $\rho_1(I,\theta,0)=0$. Eq. (2.13) can be written in the form

$$\frac{d}{dT}\rho_1(I,\theta+\Omega T,t+T)=\xi(t+T)g(I,\theta+\Omega T,t+T)+\mathcal{O}(\epsilon), \tag{2.15}$$

thus ρ_1 has a solution given by

$$\rho_1(I,\theta,t)=\int_{-t}^{0}\xi(t+T)g(I,\theta+\Omega T,t+T)dT+\mathcal{O}(\epsilon). \tag{2.16}$$

Substituting this solution into 2.12, we obtain

$$\frac{\partial\rho_0}{\partial t}+\Omega\frac{\partial\rho_0}{\partial\theta}+\epsilon^2\left(\frac{\partial H_1}{\partial I}\frac{\partial}{\partial\theta}\langle\xi(t)\rho_1\rangle-\frac{\partial H_1}{\partial\theta}\frac{\partial}{\partial I}\langle\xi(t)\rho_1\rangle\right)=0, \tag{2.17}$$

where

$$\begin{aligned}\langle \xi(t)\rho_1(I,\theta,t)\rangle &= \int_{-t}^{0} g(I,\theta+\Omega T, t+T)\langle \xi(t)\xi(t+T)\rangle dT + \mathcal{O}(\epsilon)\\ &= \sigma^2 \int_{-t}^{0} g(I,\theta+\Omega T, t+T)\delta(T)dT + \mathcal{O}(\epsilon)\\ &= -\frac{1}{2}\sigma^2\left(\frac{\partial H_1}{\partial I}\frac{\partial \rho_0}{\partial \theta} - \frac{\partial H_1}{\partial \theta}\frac{\partial \rho_0}{\partial I}\right). \end{aligned} \tag{2.18}$$

Thus, the equation for ρ_0 is finally given by

$$\begin{aligned}\frac{\partial \rho_0}{\partial t} + \Omega\frac{\partial \rho_0}{\partial \theta} &= \frac{1}{2}\epsilon^2\sigma^2\frac{\partial H_1}{\partial I}\frac{\partial}{\partial \theta}\left(\frac{\partial H_1}{\partial I}\frac{\partial \rho_0}{\partial \theta} - \frac{\partial H_1}{\partial \theta}\frac{\partial \rho_0}{\partial I}\right)\\ &\quad - \frac{1}{2}\epsilon^2\sigma^2\frac{\partial H_1}{\partial \theta}\frac{\partial}{\partial I}\left(\frac{\partial H_1}{\partial I}\frac{\partial \rho_0}{\partial \theta} - \frac{\partial H_1}{\partial \theta}\frac{\partial \rho_0}{\partial I}\right) + \mathcal{O}(\epsilon^3), \end{aligned} \tag{2.19}$$

which, neglecting the terms of order ϵ^3, is a Fokker-Planck equation. We remark that the terms $\mathcal{O}(\epsilon^3)$ can be neglected when the condition (2.3) is satisfied. Recalling the considerations made in the previous section, being θ the fast variable and I the slow variable, we assume that, in a time $t > 1/\epsilon$, the leading term is the average of ρ with respect to θ, so that we can write $\rho(I,\theta,t) \approx \rho(I,t)$, and the contribution of the derivative $\partial\rho/\partial\theta$ can be neglected. The Fokker-Planck equation then becomes

$$\frac{\partial \rho}{\partial t} = \frac{\epsilon^2\sigma^2}{2}\left\{-\left[\frac{\partial H_1}{\partial I}\frac{\partial^2 H_1}{\partial \theta^2} + \frac{\partial H_1}{\partial \theta}\frac{\partial^2 H_1}{\partial \theta \partial I}\right]\frac{\partial \rho}{\partial I} + \frac{\partial}{\partial I}\left[\left(\frac{\partial H_1}{\partial \theta}\right)^2\frac{\partial \rho}{\partial I}\right]\right\} + \mathcal{O}(\epsilon^3). \tag{2.20}$$

Taking now the average over θ we have that

$$\left\langle \frac{\partial H_1}{\partial I}\frac{\partial^2 H_1}{\partial \theta^2} + \frac{\partial H_1}{\partial \theta}\frac{\partial^2 H_1}{\partial \theta \partial I}\right\rangle_\theta = 0. \tag{2.21}$$

Thus, the final equation for the action distribution reads

$$\frac{\partial \rho}{\partial t} = \frac{\epsilon^2}{2}\frac{\partial}{\partial I}D(I)\frac{\partial \rho}{\partial I} + \mathcal{O}(\epsilon^3), \tag{2.22}$$

where the diffusion coefficient is given by

$$D(I) = \sigma^2\left\langle \left(\frac{\partial H_1}{\partial \theta}\right)^2\right\rangle_\theta. \tag{2.23}$$

To properly use Eq. (2.22), boundary conditions have to be set. A natural boundary condition at $I = 0$ exists, since in the considered model we have that

$$\lim_{I \longrightarrow 0} D(I) = 0, \tag{2.24}$$

while we need to introduce an absorbing boundary condition at $I = I_a$, which represents the presence of a collimator or, in general, the starting position of a fast escape to infinity of the particles.

2.3 Stochastic symplectic map

The stochastic symplectic maps provide models to study the effects of stochastic perturbation in particle accelerators and can be easily implemented and iterated in computer codes. Such maps simulate the effect of external fluctuating perturbations of an integrable systems using the thoery of stochastic processes. We consider the following symplectic stochastically perturbed map

$$\begin{pmatrix} x_{n+1} \\ p_{n+1} \end{pmatrix} = \begin{pmatrix} \cos\Omega(I_n) & \sin\Omega(I_n) \\ -\sin\Omega(I_n) & \cos\Omega(I_n) \end{pmatrix} \begin{pmatrix} x_n \\ p_n + \epsilon\xi_{n+1} f(x_n) \end{pmatrix}, \tag{2.25}$$

where ξ_n are random independent variables with zero mean and unit variance, ϵ is a perturbation parameter, and we define the action and angle variables as

$$x = \sqrt{2I}\sin\theta, \qquad p = \sqrt{2I}\cos\theta. \tag{2.26}$$

The function $f(x) = \mathcal{O}(x^2)$ represents the presence of non-linear terms, so that the origin is a fixed point. We assume that the integrable part is defined by the frequency

$$\Omega(I) = \omega_0 + \omega_1 I + \omega_2 \frac{I^2}{2}\,, \tag{2.27}$$

with ω_0 non-resonant. Following the approach discussed in [5], we can observe that the action dynamics can be approximated by

$$\begin{aligned} I_{n+1} = I_n &+ \epsilon\xi_{n+1}\sqrt{2I_n}\cos(\theta_n + \Omega(I_n)) f(\sqrt{2I_n}\sin(\theta_n + \Omega(I_n))) \\ &+ \frac{\epsilon^2}{2}\xi_{n+1}^2 f^2(\sqrt{2I_n}\sin(\theta_n + \Omega(I_n)))\,. \end{aligned} \tag{2.28}$$

The term $\mathcal{O}(\epsilon)$, due to the symplectic nature of the map, has the form

$$\sqrt{2I}\cos(\theta)f(\sqrt{2I}\sin(\theta)) = \frac{\partial F}{\partial \theta}(\sqrt{2I}\sin(\theta))\,, \tag{2.29}$$

where F is the primitive of f, so its angular mean value is zero. Here, we want to describe the action dynamics of this map by means of a Fokker-Planck equation. Thus, we interpret $\epsilon\xi_n(t)F(x)$ as the interpolating Hamiltonian for the following map

$$\begin{pmatrix} x_{n+1} \\ p_{n+1} \end{pmatrix} = \begin{pmatrix} x_n \\ p_n + \epsilon\xi_{n+1}f(x_n) \end{pmatrix}, \tag{2.30}$$

i.e. the perturbation Hamiltonian. We can now apply the procedure explained in the previous section and describe the action dynamics with a FP equation. To properly use the averaging theorem, we consider the fast relaxation of the angle variable, which requires the condition $\omega_2 = \mathcal{O}(1)$. This allows two orbits of the system, with different initial conditions in the angle variable, to behave as two different realisations of a stochastic process, even if we consider a single realisation of the noise ξ. This fact is relevant in the application to accelerator physics since the particles in the beam are perturbed by the same realisation of noise, but have a different initial condition in the phase space. The diffusion coefficient is then given by

$$D(I) = \left\langle \left(\frac{\partial F}{\partial \theta}(I,\theta) \right)^2 \right\rangle_\theta . \tag{2.31}$$

Chapter 3

Hollow Electron Lens for HL-LHC

Future upgrades and improvements for the CERN Large Hadron Collider (LHC) are planned and represent the mandate of the High-Luminosity project, which aims to increase the luminosity capabilities of the LHC. The upgrade, installed during the long shutdown in 2026-2028, will allow for an unprecedented total stored beam energy of about 700 MJ. Such amount of stored beam energy will need an extremely efficient collimation system, which will see the addition of the Hollow Electron Lens (HEL), to help control the beam-halo diffusion and mitigate the effects of fast beam losses. The hollow beam of electrons generated by HEL is supposed to act on the beam tails while ideally leaving the beam core unperturbed. This brief review of the HEL system describes the framework and reasons for its installation, its design, and its initial expected diffusion performances.

3.1 The need for an HEL system at the HL-LHC

The Large Hadron Collider (LHC) at the European Laboratory for Particle Physics (CERN) is a circular accelerator, installed in a 27 km long underground tunnel. It is designed to collide two 7 TeV proton beams with stored beam energies of about 362 MJ. In 2026, it is planned to start the implementation of the upgrade of the LHC according to the High-Luminosity (HL-LHC) project [1]. The aim of the upgrade is to nearly double the beam current, while reducing the beam

emittance by more than 30% with respect to the LHC design value.

The halo collimation of proton and ion beams in LHC is a key element for the machine operation. Indeed, the cryogenic nature of the LHC demands a tight control of beam losses, to minimise the energy deposited in superconducting magnets due to hadronic showers, and avoid magnet quenches. Thus, a highly-efficient collimation system is needed to minimise beam losses in the superconducting magnets and avoid damage to ring components. Although the current LHC collimation system can reach very good performance, extrapolations to HL-LHC beam conditions pose serious concerns. Sudden beam losses generated by fast transients such as orbit jitters can be naturally observed in the beam dynamics, or can have other causes, e.g. power converter ripple [17]. Even though such phenomena were under good control in Run 2, various hints of presence of overpopulated tails with respect to the typical Gaussian beam distribution, have been observed, and by simply assuming a linear scaling of the beam-halo population with the total beam current, we can estimate that, for HL-LHC, up to 36 MJ might be stored in the beam tails [18]. In addition to this, damage can also be caused in case of fast-failure scenarios, which might occur at the HL-LHC, like the operation of crab-cavities, or the risk of dumping asynchronously the two HL-LHC beams, that might trigger unwanted excitation and beam loss spikes that cannot be handled by the current collimation system alone [19].

The use of an Hollow Electron Lens (HEL) can boost the performance of the collimation system, by actively controlling the diffusion speed of the halo particles. HEL produces a low-energy hollow beam of electrons with a cylindrical symmetry that acts only on the beam halo, leaving the core nearly free of tails, thus greatly suppressing loss spikes. The electron beam runs co-axially with the hadron beam for a few meters acting at a transverse amplitude below the one of the primary collimators, so that the halo particles that are driven unstable are then safely disposed at a controllable rate.

HEL collimation system has been used already at the Fermilab Tevatron [2], where it turned out to be an effective tool to mitigate effects related to transient beam losses, while remaining compatible with the operation of the collider, and

more recently also tests at the BNL RHIC have been carried out [20].

3.2 HEL design and integration in the HL-LHC collimation system

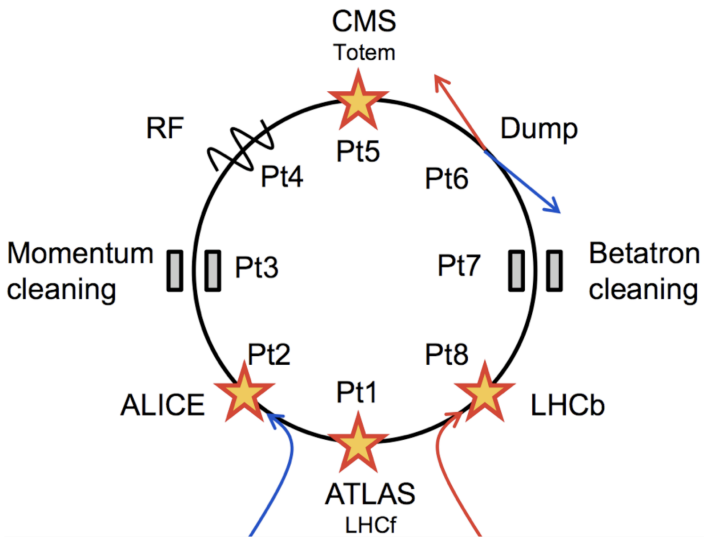

Figure 3.1: Simple representation of the LHC. The stars indicate the collision points in Pt1, Pt2, Pt5 and Pt8, where the experiments are housed. The collimation systems are in Pt3 and Pt7, while the dumping system is in Pt6. In Pt4 there is the RF system, beam instrumentation, and it is where HELs will be installed [3].

The LHC has a circumference of 27 kilometres and it has an eight-fold symmetry, with 8 arcs and 8 straight sections. As shown in Fig. 3.1, the four main experiments are installed in Pt1 (ATLAS), Pt2 (ALICE), Pt5 (CMS), and Pt8 (LHCb). The two counter-rotating beams, Beam 1 and Beam 2, are injected in Pt2 and Pt8, respectively, while the collimation systems are housed in Pt3, for momentum cleaning, and in Pt7, for betatron cleaning. In Pt6 there is the beam dumping system and, finally, in Pt4 there is a straight section housing the Radio-Frequency (RF) system and some instrumentation devices. This layout will remain unchanged for the HL-LHC. The current collimation system is organised in a precise hierarchy

based on primary collimators, secondary collimators, and absorbers, for a total of 44 movable ring collimators per beam.

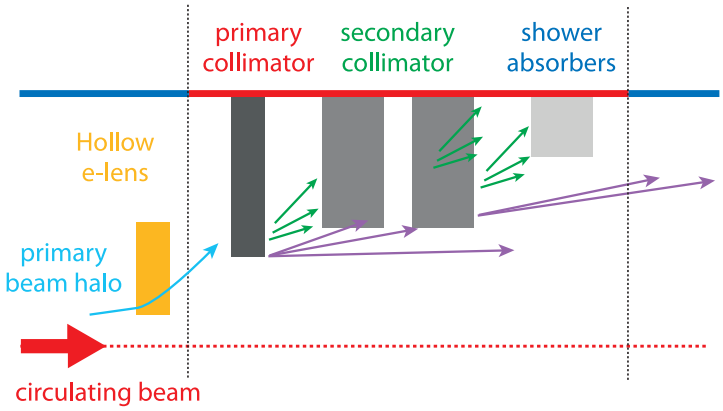

Figure 3.2: Simple scheme of the integration of the HEL in the collimation system hierarchy [3].

HELs are integrated in the transverse hierarchy of the betatron collimation system as shown in Fig. 3.2, acting on particles below the amplitude of the primary collimator jaws. HELs allow to control the diffusion speed of halo particles towards the jaws of the collimators, thus the disposal of particles remains a duty of the collimation system.

The HEL will certainly be beneficial for any type of failure scenario, however, the narrowed particle distribution after the halo depletion, may make it harder to detect critical beam losses that would require a beam dump, affecting the time margins for the Beam Loss Monitor (BLM) system. Thus, one requirement would be to leave untouched few *witness bunches* which can give rise to an early warning of a fast failure, such that the time between detection of a failure event and the beam dump remains sufficiently long [19].

The kick induced on the halo particles by means of the electromagnetic field generated by the electron beam is of the order of a fraction of a microradian. Thus, the single-turn effect is negligible and, for this reason, HELs do not need to be placed close to the collimation system [3]. The design is optimised for operation at 7 TeV, where the fast losses are a critical issue, however, it is required to start

using the HELs also during the energy ramp, so that, when the top-energy plateau is reached, the halo is already under control.

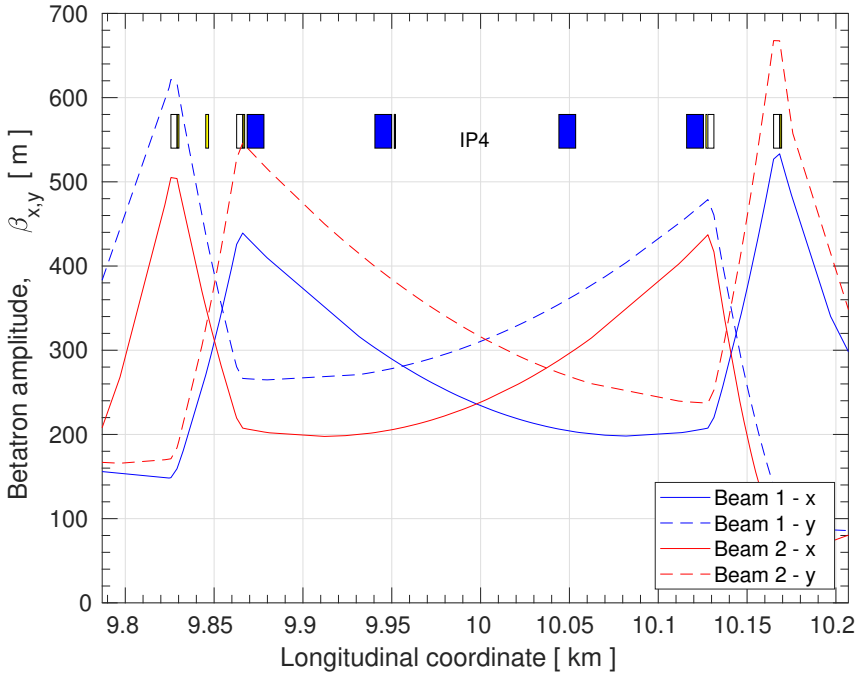

Figure 3.3: β-function evolution for both beams and both planes. The blue boxes represent dipoles and the white ones represent quadrupoles [3]

The ideal locations for the HELs were found in Pt4, near the RF system. The main reasons for this choice are the fact that Pt4 already features an independent cryogenic system (for the RF cavities) and also an increased inter-beam distance needed by the RF system, allowing for more transverse space for the HELs. More in detail, the installation points are chosen trying to generate round proton beams and increasing the β-functions, while keeping a small value of the dispersion function. The β-function for both beams around Pt4 are shown in Fig. 3.3, and HEL parameters are shown in Table 3.1. Thus, the HELs will be installed close to the "dogleg" dipoles in Pt4, where the inter-beam distance is at its maximum value of 420 mm, and the orientation of the HELs will be mirror-symmetric on the left and right side of Pt4 accounting for the opposite directions of Beam 1 and Beam 2.

The need for a cryogenic system is due to the HEL's complex design, featuring

Table 3.1: Main parameters and requirements for HEL at HL-LHC [3].

Parameter	Value/range
Proton kinetic energy, *Ebeam* [TeV]	7
Proton emittance (rms, normalized), ε^* [μm]	2.5
β-function at electron lens, $\beta_{x,y}$ [m]	280
Dispersion at electron lens, $D_{x,y}$ [m]	0.0
Proton beam size at electron lens, σ [μm]	306
Typical beam divergence (rms), σ' [μrad]	1.3-1.5
Diameter of the (warm) beam aperture, [mm]	60
Beam 1 longitudinal position from IP1, [m]	9957.0
Beam 2 longitudinal position from IP1, [m]	10037.2
Transverse scraping range at 7 TeV [σ]	>3.6
Energy range for halo scraping, E_{min} [TeV]	5
Desired 90% tail scraping time [min]	5
Tolerated proton beam core emittance blow-up [μm/h]	0.05

superconducting magnets operating at 4.5 K. The 5 T magnetic field present in the straight section is generated by 2 identical solenoid magnets. Those magnets are built around a vacuum chamber with a 60 mm inner diameter, in which a 5 A, 15 keV electron beam is driven, to interact with the proton beam over a distance of 3 m. The strong magnetic field in the straight section assures the stability and the small size of the electron beam thanks to fast Larmor oscillations around the field lines. The current design of the HEL is shown in Fig. 3.4. The design also features an electron gun and a collector to dispose of the electrons. Two tilted solenoids are placed at both sides of the main ones to steer the electron beam in and out of the proton beam. The S-design is adopted to self-compensate the edge effects of the incoming and outgoing electron beam on the core of the proton beam. However, with this design, the transverse components of the magnetic field, generated by the two steering solenoids, add up and result in a net vertical kick experienced by the proton beam. To correct this effect, a dipole corrector magnet is placed

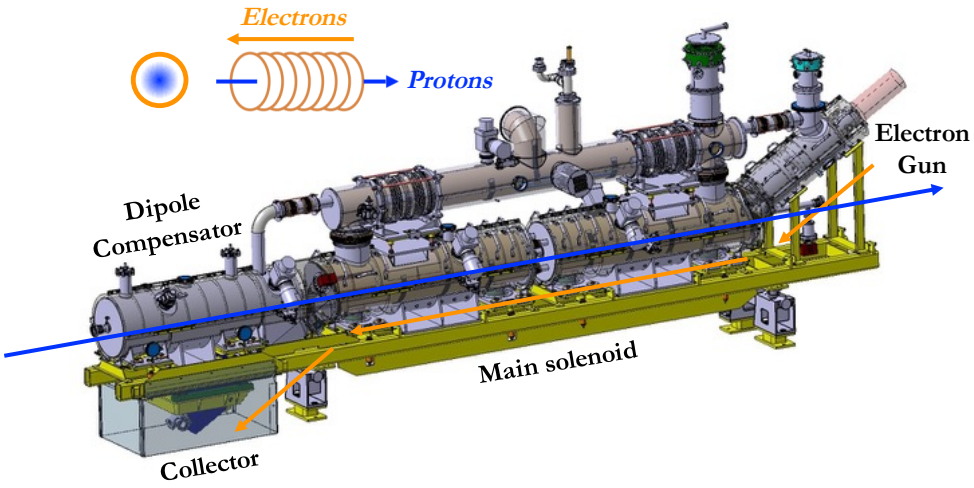

Figure 3.4: Design of the HEL for HL-LHC [4].

right before (left side in Fig.3.4). The gap between the two main solenoids contains the beam gas curtain (BGC) monitor, which can measure the transverse profile of both the proton and electron beams at the same time, relying on the fluorescence induced by the beams interacting with the gas [3].

3.3 HEL operational conditions and expected performances

HEL produces a hollow beam of electrons with an annular shape, as shown in Fig. 3.5. The cylindrical symmetry of the electron distribution is crucial to minimise residual fields in the proton beam core. The inner radius of the electron beam, r_1, determines the smallest amplitude of effect on the halo particles. The smallest inner radius for a 7 TeV beam energy is 3.6 σ, where $\sigma = \sqrt{\varepsilon\beta}$ is the RMS beam size, and the normalised emittance is assumed to be $\varepsilon^* = 2.5$ μm. Considering a nominal opening of the primary collimators of 6.7 σ, the HEL allow a clearance of about 3 σ. The outer radius of the electron beam, given by magnetic compression, is $r_2 = 2r_1$. The kick experienced by a proton of the beam when interacting with the electrons depends on its radial coordinate, and the maximum

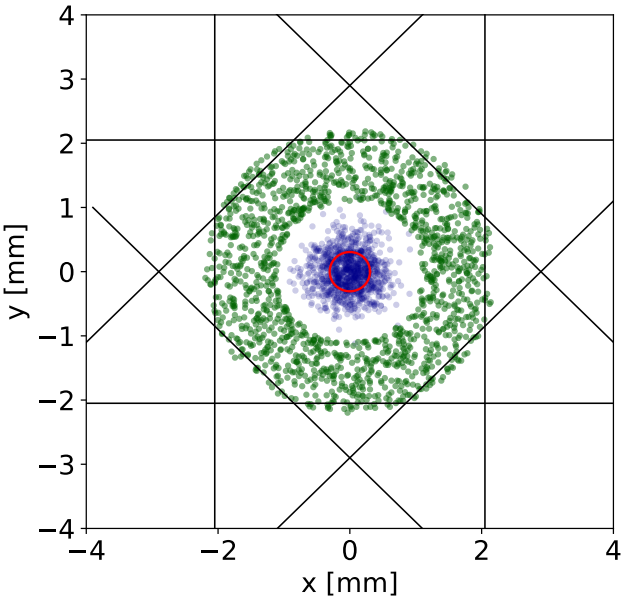

Figure 3.5: Transverse cross section of the two beams in the HEL: in blue, the Gaussian proton beam distribution, with the 1 σ envelope in red; in green, the annular distribution of electrons. The black lines indicate the nominal opening of the primary collimators [3].

transverse kick is given by

$$\theta_{\max} = \frac{1}{4\pi\epsilon_0} \frac{2\,L\,I_{\mathrm{e}}\,(1 \pm \beta_{\mathrm{e}}\beta_{\mathrm{p}})}{(B\rho)_{\mathrm{p}}\,\beta_{\mathrm{e}}\beta_{\mathrm{p}}c^2} \frac{1}{R_2}\,, \tag{3.1}$$

where where L is the length of the HEL, I_e is the electron current in Amperes, β_e and β_p are the relativistic factors for the electron and proton beams, respectively, $(B\rho)_p = 10/2.9979\ p$ GeV/c is the magnetic rigidity of the proton beam (p being the proton's momentum), ϵ_0 is the vacuum permittivity, and R_2 is the outer radius of the HEL (in mm). The + sign applies when the magnetic force is directed like the electrostatic attraction, i.e. when the electron beam moves in the opposite direction to the proton beam, whereas the − sign applies when the two beams move in the same direction. Fig. 3.6 shows the behaviour of the transverse kick as a function of the radius. In the HL-LHC configuration, for 7-TeV protons antiparallel to the electrons, with $I_e = 5$ A, $L = 3$ m, $\beta_e = 0.237$ (corresponding to 15 keV electrons), $\beta_p \sim 1$, $R_2 = 2.2$ mm, the maximum kick is $\theta_{\max} \approx 0.3$ μrad.

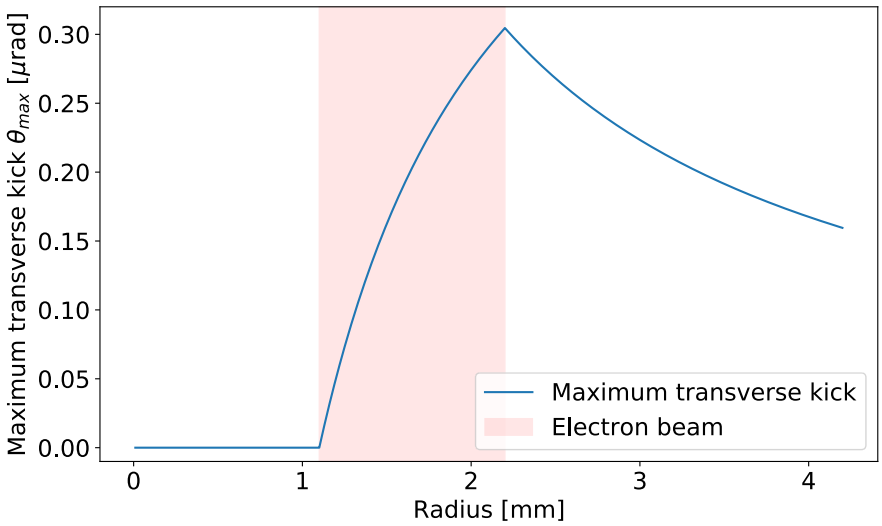

Figure 3.6: HEL transverse kick experienced by a 7 TeV proton as a function of its radial coordinate [3].

If we define the beam halo as the fraction of proton beam above r_1, and the beam core as the fraction of proton beam circulating below r_1, it is possible to determine the HEL performance by the combination of removed halo and side effects on the beam core. The larger the halo removal without inducing beam-core blow-up, the better the HEL performance. The initial estimate of the residual kick on the core is about 5 nrad for the vertical plane, and 0.1 nrad for the horizontal one. Various simulations of the HEL performance have been carried with `SixTrack` [21], that allow a detailed 6D tracking of the beam along the magnetic lattice of the machine [3, 4]. In particular Dynamic Aperture simulations and Frequency Map Analysis (FMA) have been performed to explore subsets of HEL configurations.

It is possible to switch on and off the electron beam with different patterns, on a turn-by-turn basis. Possible modulation structures that have been considered in the simulations are:

- Continuous (DC): the HEL is switched on at every turn, always with the same electron beam current.
- Random (R_p): the HEL is randomly switched on or off at every turn with a probability $p \in [0, 1]$, always with the same electron beam current.

- Pulsed (P_j^i): the HEL is switched off for j turns and on for i turns, always with the same electron beam current.
- Random current (R_I): the HEL is switched on at every turn with a current randomly chosen on a turn-by-turn basis, according to a uniform distribution of values between 0 to 5 A.

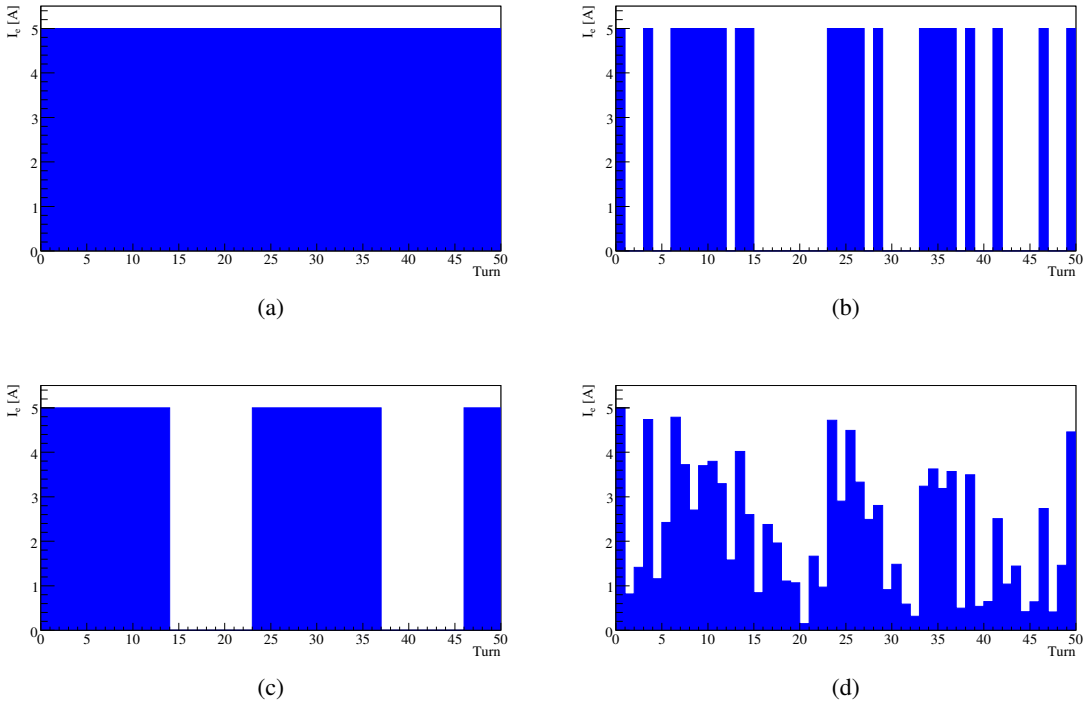

Figure 3.7: Examples of possible HEL pulsing pattern: (a) DC, (b) $R_{0.5}$, (c) P_9^{14}, (d) R_I [3].

Fig. 3.7 shows some examples of electron-pulse pattern. Studies on the Dynamic Aperture (DA) showed that, qualitatively, the closer the DA is to r_1, the more efficient is the excitation mode, while, the larger is r_1, the smaller is the difference of DA for the various pulse patterns. This can be explained considering that the nonlinear beam dynamics, at larger amplitudes, is dominated by field errors, rather than the HEL.

Overall, the most challenging pulse pattern to produce, from the hardware point

of view, is the R_I pattern. According to the `SixTrack` 6D simulations, the most efficient pattern for the halo removal is R_p, due to its spectral content (white noise). As we can see in Fig. 3.8, an almost complete halo removal is expected after about 100 s, using the pulse $R_{0.5}$, with an electron beam current of 5 A and $r_1 = 5\ \sigma$. However, an emittance blow-up, much larger than the tolerated one, is observed

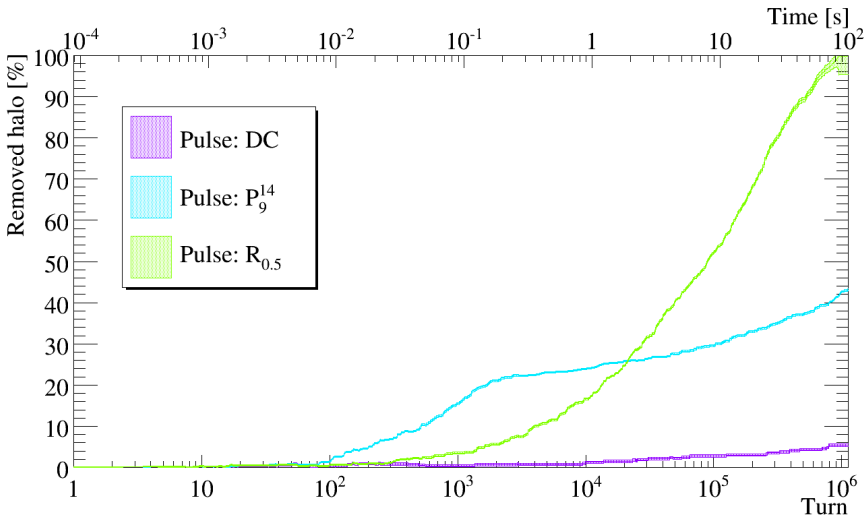

Figure 3.8: Estimated halo removal after 100 s for various HEL pulsing schemes

for such a pattern. Thus, a strategy to mitigate effects on the beam core need to be studied. For example using the random excitation with a smaller probability p, or choosing a currents 2-3 times lower than the 5 A design value, might be likely scenarios, considering that such a pulsing pattern remains effective also at lower electron beam currents.

Excitation pulses tuned to the frequency content of the beam halo were also studied, although they would be hard to implement operationally, and such an excitation window would induce an initial fast diffusion, which vanishes as soon as the particles drift outside the excitation window. Thus, the HEL frequency interval should cover all the frequencies of particles ranging from r_1 to the primary collimator.

Also the deterministic pulse P_9^{14} has been identified as a promising pattern, while the DC seems to be the least efficient, although such excitation is expected

to be more efficient when beam-beam effects are taken into account [4].

Further factors need to be considered to refine possible HEL operational scenarios, such as pulse-to-pulse stability of the electron beam, linear coupling, and dependence on the betatron tune. The tune footprint is affected by the head-on beam-beam effect, and further studies will follow to demonstrate the performance of the DC and P_j^i pulsing patterns when beam-beam effects are involved.

Obviously, the HL-LHC operational cycle and lattice are still subjected to modifications, however, no major changes are expected for the non-colliding beams in the results already carried out.

Chapter 4

An HEL Simple Model

The simple model presented here is a useful tool to study the behaviour of the beam dynamics when an hollow electron lens, discussed in the previous section, is used to control the tails population. We modelled the phenomenon as a diffusion process, described by a diffusion equation, and we made use of this model to explore various operational scenarios, and possibly, search for the most efficient way to have a fast beam cleaning. Several tracking simulations were performed and the results were compared to the solutions of a Fokker-Planck equation, computed by a Crank-Nicolson integrator. Although the model was derived for the 4D scenario, most of the simulations were performed for the 2D case, in order to have a simplified model to make comparisons with the FP solutions. Various kinds of noise were studied and applied to perturbe the system, in order to probe the model in different scenarios, and to show the validity of the diffusion approximation.

4.1 HEL transfer map

The 4D one-turn transfer map of a circular accelerator including localised sources of nonlinearities can be written as:

$$\begin{pmatrix} X \\ X' \\ Y \\ Y' \end{pmatrix}_{n+1} = \mathbf{M} \begin{pmatrix} X \\ X' + f_x(X,Y) \\ Y \\ Y' + f_y(X,Y) \end{pmatrix}_{n} , \tag{4.1}$$

where (X, X', Y, Y') is a vector in the 4D phase space representing the particle's coordinates at the entrance of the element generating the non-linear force. $\mathbf{M}$ is a 4×4 matrix in block-diagonal form, namely

$$\mathbf{M} = \begin{pmatrix} \mathbf{M}_x & 0 \\ 0 & \mathbf{M}_y \end{pmatrix} \tag{4.2}$$

$\mathbf{M}_{x,y}$ being 2×2 matrices and the functions f_x, f_y are related to the nonlinearities in the machine.

It is customary to change coordinates from physical to Courant-Snyder ones. As said in [10], this is obtained by means of the linear, symplectic transformation:

$$\begin{pmatrix} z \\ \\ z' \end{pmatrix} = \mathbf{T}_z^{-1} \begin{pmatrix} Z \\ \\ Z' \end{pmatrix}, \qquad \mathbf{T}_z = \begin{pmatrix} \sqrt{\beta_z} & 0 \\ \\ -\dfrac{\alpha_z}{\sqrt{\beta_z}} & \dfrac{1}{\sqrt{\beta_z}} \end{pmatrix} , \tag{4.3}$$

where z stands for x or y and the quantities α_z, β_z are the Twiss parameters at the location of the nonlinear element. The general 4D normalisation matrix $\mathbf{T}$ is in block diagonal form,

$$\mathbf{T} = \begin{pmatrix} \mathbf{T}_x & 0 \\ 0 & \mathbf{T}_y \end{pmatrix} . \tag{4.4}$$

By taking into account that

$$\mathbf{R}(\omega_x, \omega_y) = \mathbf{T}^{-1}\,\mathbf{M}\,\mathbf{T}, \qquad \mathbf{R}(\omega_x, \omega_y) = \begin{pmatrix} \mathbf{R}(\omega_x) & 0 \\ 0 & \mathbf{R}(\omega_y) \end{pmatrix} , \tag{4.5}$$

with $\mathbf{R}(\omega_z)$ a 2×2 rotation matrix

$$R(\omega_z) = \begin{pmatrix} \cos\omega_z & \sin\omega_z \\ -\sin\omega_z & \cos\omega_z \end{pmatrix}, \qquad \omega_z = 2\pi\nu_z\,, \tag{4.6}$$

the mapping (4.1) reads in the new coordinates:

$$\begin{pmatrix} x \\ x' \\ y \\ y' \end{pmatrix}_{n+1} = \mathbf{R}(\omega_x, \omega_y) \begin{pmatrix} x \\ x' + \sqrt{\beta_x} f_x\left(\sqrt{\beta_x}x, \sqrt{\beta_y}y\right) \\ y \\ y' + \sqrt{\beta_y} f_y\left(\sqrt{\beta_x}x, \sqrt{\beta_y}y\right) \end{pmatrix}_{n}. \tag{4.7}$$

The optical conditions at the planned location of the HEL are such that $\beta_x = \beta_y = 280$ m, hence, Eq. (4.7) can be simplified as

$$\begin{pmatrix} x \\ x' \\ y \\ y' \end{pmatrix}_{n+1} = \mathbf{R}(\omega_x, \omega_y) \begin{pmatrix} x \\ x' + \sqrt{\beta} f_x\left(\sqrt{\beta}x, \sqrt{\beta}y\right) \\ y \\ y' + \sqrt{\beta} f_y\left(\sqrt{\beta}x, \sqrt{\beta}y\right) \end{pmatrix}_{n}, \tag{4.8}$$

and it is easy to show that the physical radial coordinate is $R = \sqrt{\beta}\, r$, where $r = \sqrt{x^2 + y^2}$ is the normalised radius.

It is worth noting that after the transformation of the physical co-ordinates to normalised ones, the units are $\sqrt{m}$. It is useful to transform the physical coordinates to dimensionless normalised coordinates. This can be obtained by using the following form for the normalising transformation $\mathbf{T}_z$, where ε is the physical beam emittance

$$\mathbf{T}_z = \begin{pmatrix} \sqrt{\beta_z\,\varepsilon} & 0 \\ -\alpha_z\sqrt{\dfrac{\varepsilon}{\beta_z}} & \sqrt{\dfrac{\varepsilon}{\beta_z}} \end{pmatrix}, \tag{4.9}$$

which corresponds to using coordinates expressed in units of beam size. Finally,

Eq. (4.8) can be rewritten as

$$\begin{pmatrix} x \\ x' \\ y \\ y' \end{pmatrix}_{n+1} = \mathbf{R}(\omega_x, \omega_y) \begin{pmatrix} x \\ x' + \sqrt{\dfrac{\beta}{\varepsilon}} f_x\left(\sqrt{\beta\varepsilon}\, x, \sqrt{\beta\varepsilon}\, y\right) \\ y \\ y' + \sqrt{\dfrac{\beta}{\varepsilon}} f_y\left(\sqrt{\beta\varepsilon}\, x, \sqrt{\beta\varepsilon}\, y\right) \end{pmatrix}_n . \tag{4.10}$$

The model to describe the beam dynamics under the effect of the nonlinearities of the ring and of the HEL is based on the following 4D map (see appendix A for the derivation of the expression of the kick):

$$\begin{pmatrix} x \\ p_x \\ y \\ p_y \end{pmatrix}_{n+1} = \begin{pmatrix} \mathbf{R}(\Omega_x(I_{x,n}, I_{y,n})) & 0 \\ 0 & \mathbf{R}(\Omega_y(I_{x,n}, I_{y,n})) \end{pmatrix} \begin{pmatrix} x \\ p_x + \xi_{n+1}\, \hat{\theta}(r)\, \dfrac{x}{r} \\ y \\ p_y + \xi_{n+1}\, \hat{\theta}(r)\, \dfrac{y}{r} \end{pmatrix}_n \tag{4.11}$$

where ξ_n is a randomly distributed variable with finite variance σ^2, representing a noise that justifies the diffusive approach, and

$$\hat{\theta}(r) = \sqrt{\frac{\beta}{\varepsilon}}\, \hat{\theta}_{\max}\, \frac{f(r)}{(r/r_2)}\,, \tag{4.12}$$

with the maximum kick $\hat{\theta}_{\max}$ given by [22]

$$\hat{\theta}_{\max} = \frac{1}{4\pi\epsilon_0} \frac{2\, L\, I_{\mathrm{e}}\, (1 \pm \beta_{\mathrm{e}}\beta_{\mathrm{p}})}{(B\rho)_{\mathrm{p}}\, \beta_{\mathrm{e}}\beta_{\mathrm{p}} c^2} \frac{1}{R_2}\,, \tag{4.13}$$

which is the same as Eq. (3.1), while the function $f(r)$, in this model, is expressed as

$$f(r) = \begin{cases} 0\,, & r < r_1 \\ \dfrac{r^2 - r_1^2}{r_2^2 - r_1^2}\,, & r_1 \le r < r_2 \\ 1\,, & r \ge r_2 \end{cases} \tag{4.14}$$

where $r_1 < r_2$ represent the inner and outer radius of the electron beam, respectively, expressed in units of beam size, and usually $r_2 = 2r_1$. All kick parameters are shown in Tab. 4.1.

Table 4.1: Kick parameters for the HEL transfer map.

Parameter	Value
Proton kinetic energy, E_{beam} [TeV]	7
Proton emittance (rms, normalized), $\varepsilon^*_{\text{ref}}$ [μm]	2.5
β-function at electron lens, $\beta_{x,y}$ [m]	28
Inner HEL radius, r_1 [σ_{beam}]	>3.6
Electron beam current, I_e [A]	5
Length of HEL, L [m]	3
Electrons relativistic factor, β_e	0.237

In the rotation matrices, the linear actions have been introduced, which are defined as

$$I_z = \frac{z^2 + p_z^2}{2} \tag{4.15}$$

and the functions $\Omega_z(I_x, I_y)$ represent the amplitude detuning, namely

$$\begin{aligned}
\Omega_x(I_x, I_y) &= \omega_{x,0} + \frac{\partial \Omega_x}{\partial I_x} I_x + \frac{\partial \Omega_x}{\partial I_y} I_y + \frac{1}{2}\left(\frac{\partial^2 \Omega_x}{\partial I_x^2} I_x^2 + \frac{\partial^2 \Omega_x}{\partial I_x \partial I_y} 2 I_x I_y + \frac{\partial^2 \Omega_x}{\partial I_y^2} I_y^2\right) + \cdots \\
\Omega_y(I_x, I_y) &= \omega_{y,0} + \frac{\partial \Omega_y}{\partial I_x} I_x + \frac{\partial \Omega_y}{\partial I_y} I_y + \frac{1}{2}\left(\frac{\partial^2 \Omega_y}{\partial I_x^2} I_x^2 + \frac{\partial^2 \Omega_y}{\partial I_x \partial I_y} 2 I_x I_y + \frac{\partial^2 \Omega_y}{\partial I_y^2} I_y^2\right) + \cdots .
\end{aligned} \tag{4.16}$$

The coefficients can be computed by means of a tracking code, but in this case, the coefficients representing the derivatives of the tunes with respect to the beam emittances are provided. Typical values corresponding to HL–LHC operational

conditions are [23]

$$\begin{aligned}
&\frac{\omega_{x,0}}{2\pi} = 0.31 && \frac{\omega_{y,0}}{2\pi} = 0.32 \\
&\frac{1}{2\pi}\frac{\partial\Omega_x}{\partial\varepsilon_x} \approx -1.73\times10^5 && \frac{1}{2\pi}\frac{\partial\Omega_x}{\partial\varepsilon_y} \approx 0.92\times10^5 && \frac{1}{2\pi}\frac{\partial\Omega_y}{\partial\varepsilon_y} \approx -0.77\times10^5 \\
&\frac{1}{2\pi}\frac{\partial^2\Omega_x}{\partial\varepsilon_x^2} \approx -1.87\times10^{12} && \frac{1}{2\pi}\frac{\partial^2\Omega_x}{\partial\varepsilon_x\partial\varepsilon_y} \approx 0.66\times10^{12} && \frac{1}{2\pi}\frac{\partial^2\Omega_x}{\partial\varepsilon_y^2} \approx -1.49\times10^{12} \\
&\frac{1}{2\pi}\frac{\partial^2\Omega_y}{\partial\varepsilon_y^2} \approx -3.36\times10^{12}\,,
\end{aligned} \tag{4.17}$$

where the following identities were used to determine the missing coefficients

$$\frac{\partial\Omega_y}{\partial\varepsilon_x} = \frac{\partial\Omega_x}{\partial\varepsilon_y} \qquad \frac{\partial^2\Omega_y}{\partial\varepsilon_x^2} = \frac{\partial^2\Omega_x}{\partial\varepsilon_x\partial\varepsilon_y} \qquad \frac{\partial^2\Omega_y}{\partial\varepsilon_x\partial\varepsilon_y} = \frac{\partial^2\Omega_x}{\partial\varepsilon_y^2}\,. \tag{4.18}$$

The numerical coefficients given in Eqs. (4.18) need to be converted into action values to be used in Eq. (4.16). The standard relationship is given by

$$\varepsilon_z = 2I_z\,, \tag{4.19}$$

however, in our case the action used is defined in special dimensionless coordinates, which means that Eq. (4.19) should be replaced by

$$\varepsilon_z = 2\frac{\varepsilon^*_{\mathrm{ref}}}{\beta_{\mathrm{p}}\gamma_{\mathrm{p}}}I_z\,, \tag{4.20}$$

and the derivatives needed in Eq. (4.16) should be evaluated by means of the chain rule

$$\frac{\partial^n}{\partial\varepsilon_z^n} = \left(\frac{\partial I_z}{\partial\varepsilon_z}\right)^n\frac{\partial^n}{\partial I_z^n} \qquad \text{and} \qquad \frac{\partial I_z}{\partial\varepsilon_z} = \frac{\beta_{\mathrm{p}}\gamma_{\mathrm{p}}}{2\varepsilon^*_{\mathrm{ref}}} \tag{4.21}$$

to use the coefficients given in Eqs. (4.18).

4.2 Diffusion model for HEL

We consider the stochastically perturbed symplectic map of Eq. (4.11), and we define the action angle variable as

$$z = \sqrt{2I_z}\sin\phi_z \qquad p_z = \sqrt{2I_z}\cos\phi_z\,. \tag{4.22}$$

By applying the approach discussed in chapter 2, one obtains the following equations

$$\begin{aligned}
I_{x,n+1} &= I_{x,n} + \xi_{n+1}\frac{\hat{\theta}(r_n)}{r_n}2I_{x,n}\cos\left(\phi_{x,n}+\Omega_x(I_{x,n},I_{y,n})\right)\times \\
&\times \sin\left(\phi_{x,n}+\Omega_x(I_{x,n},I_{y,n})\right) + \frac{1}{2}\xi_{n+1}^2\frac{\hat{\theta}^2(r_n)}{r_n^2}\times \\
&\times 2I_{x,n}\sin^2\left(\phi_{x,n}+\Omega_x(I_{x,n},I_{y,n})\right) \\
I_{y,n+1} &= I_{y,n} + \xi_{n+1}\frac{\hat{\theta}(r_n)}{r_n}2I_{y,n}\cos\left(\phi_{y,n}+\Omega_y(I_{x,n},I_{y,n})\right)\times \\
&\times \sin\left(\phi_{y,n}+\Omega_y(I_{x,n},I_{y,n})\right) + \frac{1}{2}\xi_{n+1}^2\frac{\hat{\theta}^2(r_n)}{r_n^2}\times \\
&\times 2I_{y,n}\sin^2\left(\phi_{y,n}+\Omega_y(I_{x,n},I_{y,n})\right)
\end{aligned} \tag{4.23}$$

where $r_n = \sqrt{2I_{x,n}\sin^2\left(\phi_{x,n}+\Omega_x(I_{x,n},I_{y,n})\right)+2I_{y,n}\sin^2\left(\phi_{y,n}+\Omega_y(I_{x,n},I_{y,n})\right)}$.

We now simplify the system by considering only the motion in one plane. Then, limiting the analysis to the motion in the horizontal plane, i.e. imposing $I_y = 0$, reduces Eq (4.23) to

$$\begin{aligned}
I_{n+1} &= I_n + \xi_{n+1}\hat{\theta}(\sqrt{2I_n}\sin\left(\phi_n+\Omega(I_n)\right))\sqrt{2I_n}\cos\left(\phi_n+\Omega(I_n)\right)+ \\
&+ \frac{1}{2}\xi_{n+1}^2\hat{\theta}^2(\sqrt{2I_n}\sin\left(\phi_n+\Omega(I_n)\right))\,.
\end{aligned} \tag{4.24}$$

Then, we consider that

$$\hat{\theta}(\sqrt{2I}\sin\phi)\sqrt{2I}\cos\phi = \frac{\partial F}{\partial\phi}(\sqrt{2I}\sin\phi), \tag{4.25}$$

and we interpret $\xi(t)F(x)$ as the interpolating perturbation Hamiltonian.

Then, the dynamics generated by the map (4.11) can be represented by a Fokker-Plank equation in which the diffusion coefficient is given by

$$D(I) = \sigma^2\left(\frac{\hat{\theta}_{\max}R_2}{\varepsilon}\right)^2\left\langle\left[\sqrt{2I}\cos\phi\,\frac{f\left(\sqrt{2I}\sin\phi\right)}{\sqrt{2I}\sin\phi}\right]^2\right\rangle_\phi . \tag{4.26}$$

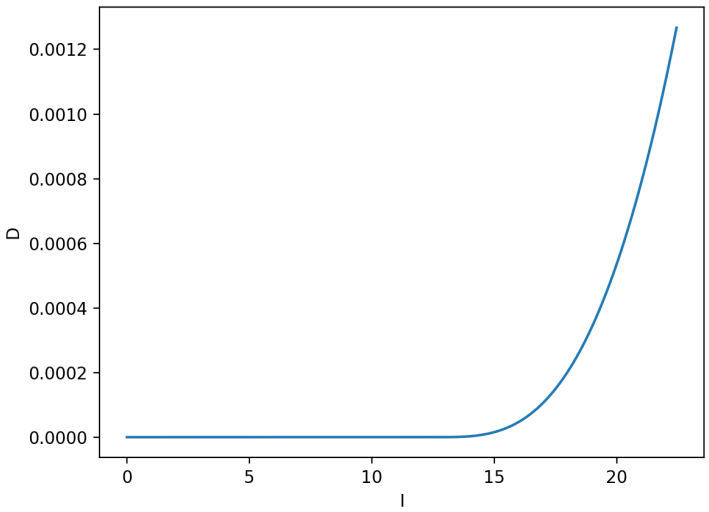

Figure 4.1: Example of diffusion coefficient as a function of I, computed for $r_1 = 5\ \sigma_{\text{beam}}$ and $\sigma^2 = 0.25$. Here the action is in units of $\sigma^2_{\text{beam}}/2$.

Since the only angular terms are $\sin^2\phi$ and $\cos^2\phi$, we can consider only the positive quadrant of the phase space, therefore we obtain

$$D(I) = \sigma^2 \left(\frac{\hat{\theta}_{\max} R_2}{\varepsilon} \right)^2 \frac{2}{\pi} \int_0^{\pi/2} \left(\frac{f(\sqrt{2I}\sin\phi)}{\tan\phi} \right)^2 d\phi \,. \tag{4.27}$$

An example of the behaviour of the diffusion coefficient is shown in Fig. 4.1

4.3 Beyond the white noise

One of the aims of this work was to study the diffusion process of the electron lens in order to find specific conditions that could enhance the diffusion, and allow for a faster and more efficient halo depletion. Obviously acting on the noise by varying its variance, has a large impact on the diffusion. Indeed, we expect to observe the largest diffusion when the noise with the largest variance is chosen. However, it is possible to further enhance the diffusion by considering a noise that is not white but rather correlated, i.e. with specific Fourier components in its

spectrum. Indeed, it is possible to induce resonances between the spectral density of the noise and the proper frequencies of the system, considering the resonance condition

$$\omega = k\Omega(I) - 2\pi l\,, \qquad k, l \in \mathbb{Z} \tag{4.28}$$

where Ω and ω are respectively the frequency of the system and the main spectral components of the correlated noise, multiplied by 2π. Note that, for a given k, this holds true for every l, because, for the discrete HEL transfer map, the sampling frequency of the noise is $f_\mathrm{s} = 1$, and every frequency exceeding $f_\mathrm{s}/2$ is subjected to the aliasing effect. For different values of k it is possible to find specific values ω^* that excite a resonance in the system. This has a large impact on the diffusion coefficient. As shown in [25, 26], if one expresses the perturbation Hamiltonian as a Fourier expansion

$$H_1(I, \theta) = \sum_k h_k(I) e^{ik\theta}\,, \tag{4.29}$$

it is then possible to write the diffusion coefficient as (see [25] for the derivation)

$$D(I) = \sum_k k^2 |h_k(I)|^2 \tilde{\phi}(k\Omega(I)) \tag{4.30}$$

where $\tilde{\phi}(\omega)$ is the spectral density of the noise. As discussed in [26], the amplitudes $\tilde{\phi}(\omega)$ contributes to $D(I)$ when the frequencies $\omega^* = k\Omega(I)$ are present in the Fourier expansion of the perturbation (4.29). In the case of white noise, $\tilde{\phi}(\omega)$ is constant, and the diffusion coefficient reduces to

$$D(I) = \sum_k k^2 |h_k(I)|^2\,. \tag{4.31}$$

Then, if a noise, with the same power, is peaked on ω^*, more power will be given to the frequencies that contribute to $D(I)$ and, as a result, the diffusion coefficient will be larger.

Chapter 5

Simulation Details

In this chapter, we express various details of the simulations of the HEL system. In particular the distribution of the initial conditions of halo particles is explicated. We express the various choices of white noise, and we dwell on the generation of the colored noises. In the end, we show few preliminary studies of the system.

5.1 Initial conditions

The hollow electron lens is planned to be implemented in the HL-LHC collimation system to mitigate the fast beam loss due to overpopulated tails. Indeed, the tails show a particles population higher than expected from an usual Gaussian distribution. For this reason, here we consider a particle distribution given by two overlapping Gaussians:

$$\rho(x) = \frac{A_1}{\sqrt{2\pi\sigma_1^2}} \exp\left\{-\frac{1}{2}\left(\frac{x-\mu_1}{\sigma_1}\right)^2\right\} + \frac{A_2}{\sqrt{2\pi\sigma_2^2}} \exp\left\{-\frac{1}{2}\left(\frac{x-\mu_2}{\sigma_2}\right)^2\right\}, \quad (5.1)$$

with equal mean $\mu_1 = \mu_2 = 0$, standard deviations $\sigma_1 = 1\ \sigma_{\text{beam}}$, $\sigma_2 = 2\ \sigma_{\text{beam}}$ and with contributions $A_1 = 0.65$ and $A_2 = 0.35$.

The same distribution is considered for the momentum coordinate p_x. This translates into an uniform distribution in the angle variable, and an initial action distribution of the form

$$\rho(I) = \frac{1}{\Gamma}\left(\frac{A_1}{\sigma_1^2}\exp\left\{-\frac{I}{\sigma_1^2}\right\} + \frac{A_2}{\sigma_2^2}\exp\left\{-\frac{I}{\sigma_2^2}\right\}\right), \quad (5.2)$$

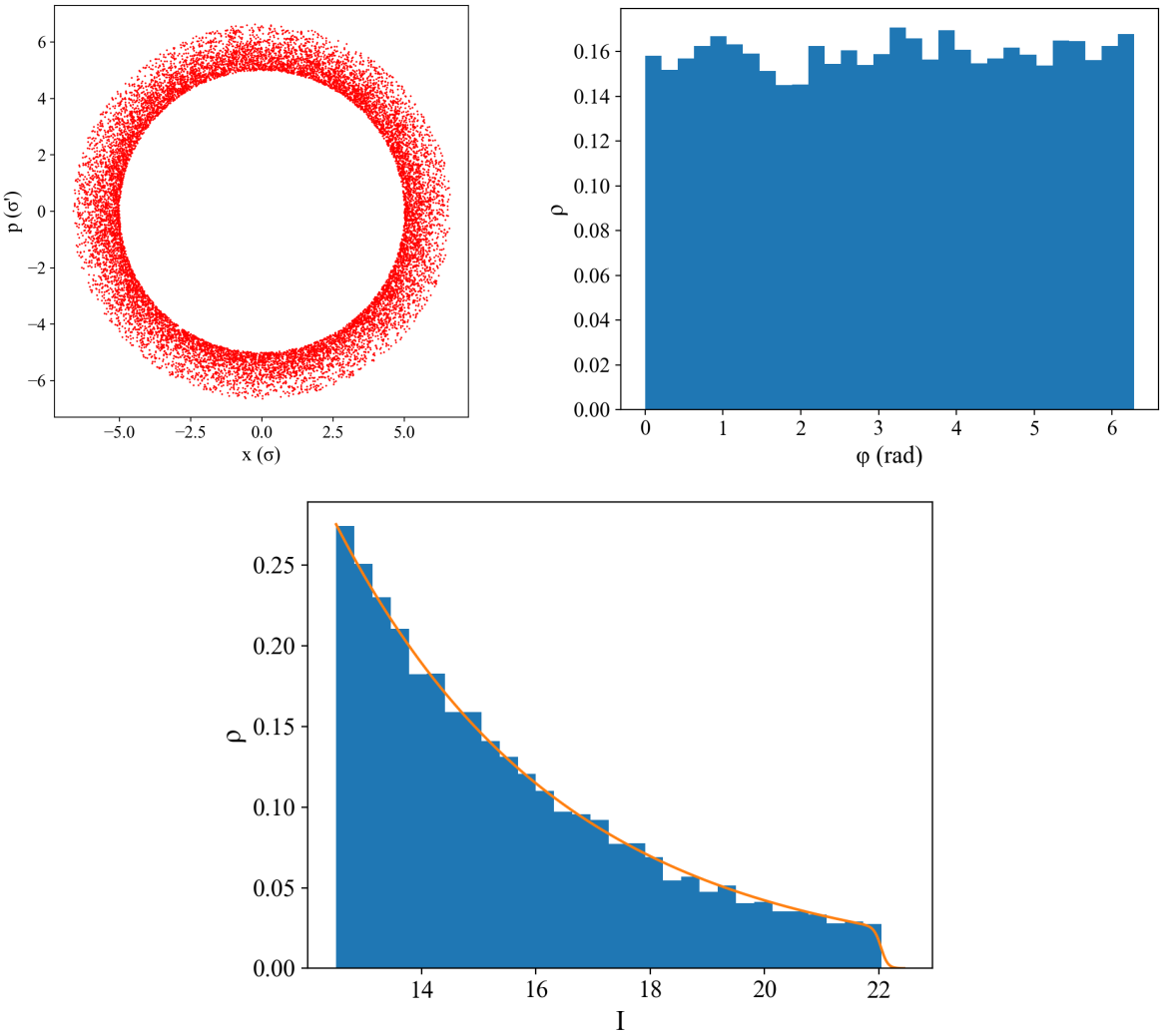

Figure 5.1: Example of initial conditions for $r_1 = 5\ \sigma_{\text{beam}}$ and $r_a = 6.7\ \sigma_{\text{beam}}$. (top left) Phase space of initial conditions of the halo particles; (top right) corresponding angle variable distribution. (bottom) Initial action distribution: in blue, the actual histogram distribution, while the yellow line represents the analytic function of the distribution (Eq. (5.2)), with a logistic damping towards the the boundary condition. Here the action is in units of $\sigma^2_{\text{beam}}/2$.

where Γ is a normalization factor. Thus, the initial conditions start with the angle variable already relaxed, so that we can describe the evolution of the system only

by means of the action variable using a FP equation.

We define the beam core as all the particles whose action is $I < r_1^2/2$, and halo all the particle whose action is $r_1^2/2 \leq I < r_a^2/2$, where r_1 is the HEL inner radius, and r_a is the absorbing barrier radius of the primary collimator, that defines the boundary condition for the action distribution $I_a = r_a^2/2$. Then all particles located beyond the absorbing barrier are removed from the initial conditions.

Furthermore, given the large number of calculations needed to perform a complete simulation of large amounts of particles, and the fact that we consider a zero HEL field on the beam core, we also perform a further cut on the initial conditions by considering only the halo particles in the simulations.

An example of typical initial conditions for a 2D (only the horizontal plane is considered) simulation, starting from a total number of beam particles of 10^6, is given in Figs. 5.1

5.2 Choice of white noises

To simulate a diffusive process, various types of white noise were generated. To be physical, and compatible with the HEL case, the noise always need to have a value between 0 and 1. Thus, for example, we could not use a normal distribution, and only limited distributions have been considered. The white noise distributions studied are the following:

- $R_p[a, b]$: the noise has a Bernoulli distribution in the domain $[a, b]$, where $a < b \in [0, 1]$, p is the probability to assume the value b and $(1 - p)$ is the probability assume the value a.
- R_I: the noise has a uniform distribution in [0,1]
- M_λ: the noise has a distribution created by means of a Markov chain and represents a middle ground between the previous two noise distributions. More in detail, a Metropolis-Hastings algorithm was used to generate a distribution of the form

$$\rho(\xi) = \frac{e^{-\lambda\xi} + e^{\lambda(\xi-1)}}{\frac{2}{\lambda}(1 - e^{-\lambda})} \qquad \xi \in [0, 1] \tag{5.3}$$

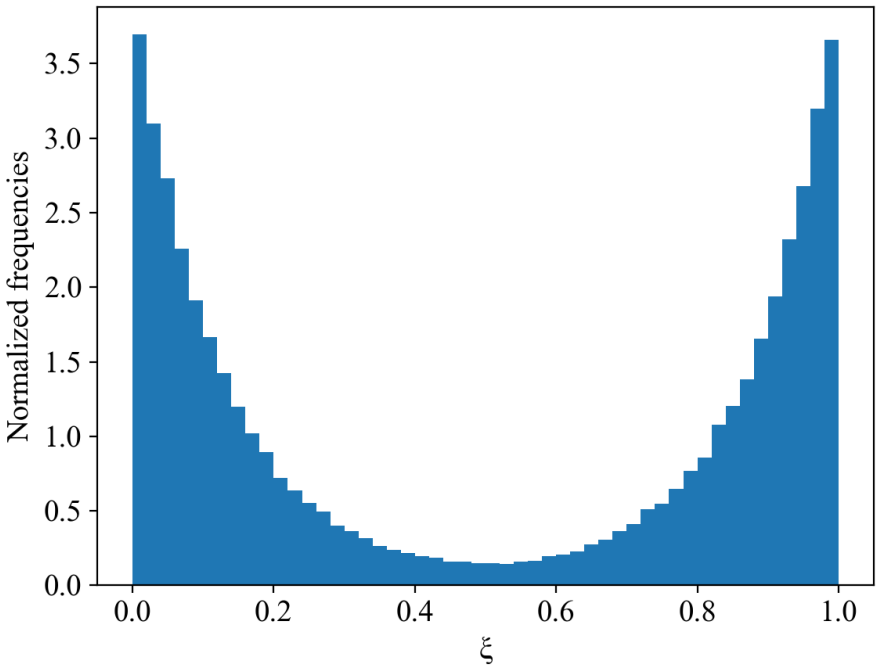

Figure 5.2: Example of noise generated following the distribution of Eq. (5.3), where $\lambda = 8$.

where λ is a parameter of choice. Then, a shuffle of the noise was performed to remove the correlation, and make it white. An example of such distribution is shown on Fig. 5.2. With this particular noise, it is possible to change the variance by varying the parameter λ.

5.3 Generation of correlated noise

Besides the white noises, we also looked for a way to generate a noise that allowed for the maximum diffusion. The noise had to satisfy many conditions, namely:

- it had to be physical, which means that it could contain only values in the $[0, 1]$ interval;

- it had to have the maximum allowed variance in such interval, which is equal to 0.25, achievable using the noise $R_{0.5}[0,1]$ (Bernoulli distribution);
- it had to be colored, which means that its frequency spectrum had to show a peak covering specific interval of frequencies, in order to induce resonances that could enhance the diffusion.

Thus, a noise with a distribution $R_{0.5}[0,1]$ with the right Fourier components seemed ideal. However, all these specific conditions did not allow us to use the standard tools to generate a correlated noise, like noise filters or band limited noises. Hence, I came up with a simple algorithm to generate an ad hoc noise that satisfy all the previous conditions. The trade off of this noise is its limited viability interval of frequencies, and its low consistency along such interval, that caused differences in the profiles of the frequency spectrum for different noises.

We remark that, every time we talk about frequencies, we are not referring to s^{-1}, but rather to n_{t}^{-1}, where n_{t} are the machine turns. Thus, here the frequency is a dimensionless quantity.

We will now give few details of the generation of the ad hoc noise. Given a desired frequency ω, the algorithm searches for the two square waves with the nearest frequencies. Then, it combines such square waves, appending one after the other. The choice of the subsequent wave to append is made with a specific probability, calculated with a weighted mean of the two frequencies, in order to obtain a final signal with a specific frequency lying between the two. This allows us to generate a signal that is still a noise, giving the random choice of the waves, but that is peaked on the desired frequency. To maintain the right variance, every time a wave with an odd period is chosen, the algorithm also makes another random choice on the number of $1s$ and $0s$ of the wave. For example, for the noise shown in Fig 5.3, we aimed for $\omega/2\pi = 0.24$, thus we mixed the square wave with period 4, [1,1,0,0], and one with period 5, which was randomly selected every time between [1,1,0,0,0] and [1,1,1,0,0]. In this way we can generate a correlated noise with the maximum possible variance.

The viable range of frequency of this noise is between 0.11 and 0.34. Outside these values, the noise becomes too much or not enough correlated. While here,

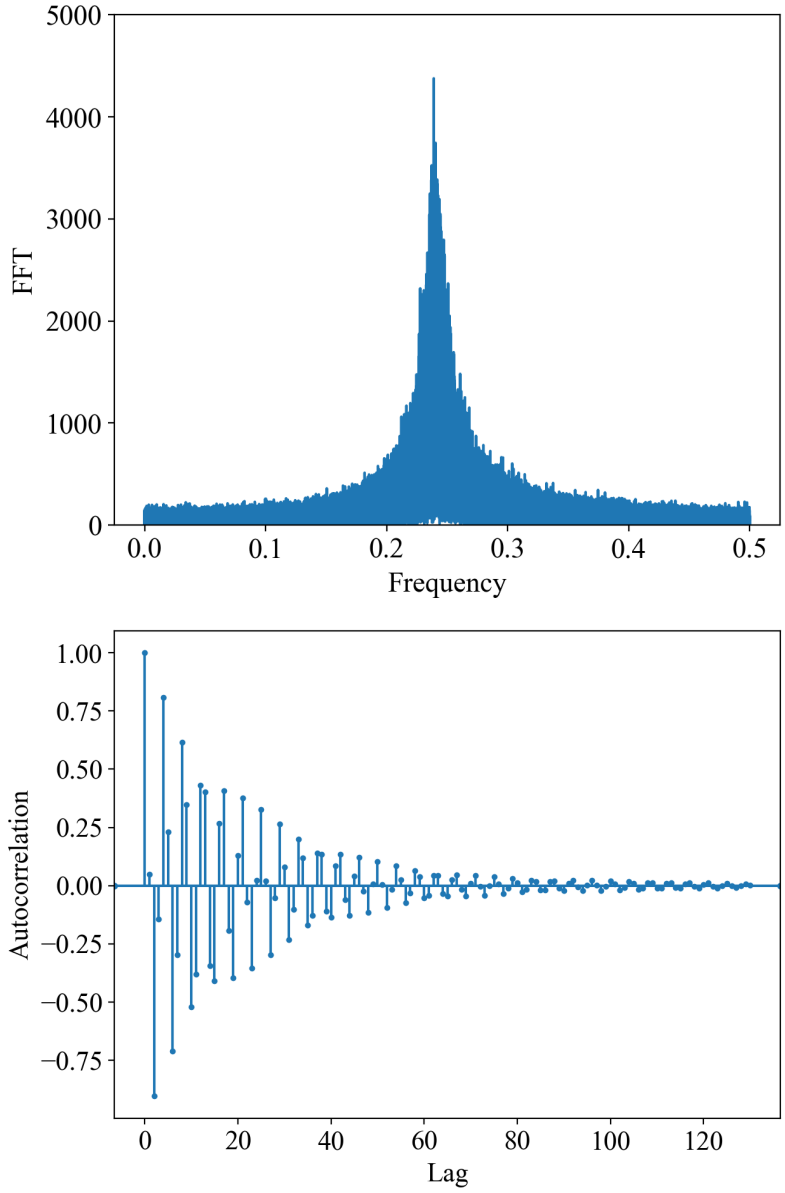

Figure 5.3: FFT (top) and autocorrelation (bottom) of the ad hoc noise with a frequency peak at 0.24, generated using square waves with period 4 and 5.

we were just searching for the noise that could enhance the most the diffusion, an optimised and complete study on the HEL diffusion with, more consistent, correlated noises, has to be performed in the future.

5.4 Preliminary studies

We tested various simulations without noise to probe the tune of the map. We also searched for resonances induced by the presence of noise with a mean larger than 0. We performed few tracking simulations of the map, applying only a mean value of the noise, to see the effect on the tunes and phase space. An example of a study of the 2D map tune is shown in Fig. 5.4, where we can see that the system is basically linear. Indeed, in the simplified model we built, the nonlinearities of the machine are considered integrable. Then, the only effect of the nonlinearities is a tuneshift expressed in Eq. (4.16), without causing any instability in the motion. Such simplification translates into a system which results to be extremely linear. Indeed no relevant inherent resonance was found, neither in the 2D system nor the 4D one. Such system linearity is also responsible for large fluctuations in the particle loss current, which disappear when a different set of machine tune values is chosen, or a personal noise, different for every particle, is selected.

The possibility to enhance the diffusion by inducing resonances in the system using a time-correlated noise was also considered. We performed few 2D tracking simulations of the map where, instead of noise, we applied a sinusoidal signal with the frequency necessary to satisfy the resonant condition of Eq. (4.28), and mean 0.5. An example of that can be seen in Fig. 5.5 , in which

$$\omega = 4\Omega(I_{\mathrm{h}}) - 2\pi\,, \tag{5.4}$$

where I_{h} refers to the action in the halo region. Fig. 5.5 clearly shows a phase locking in the halo region, which is a sign of the presence of the resonance induced by the sinusoidal signal. We performed this study for k up to 6, and we found resonances of order 2, 4 and 6. This is explained by the presence of only those specific components in the Fourier expansion of the perturbation Hamiltonian (4.29).

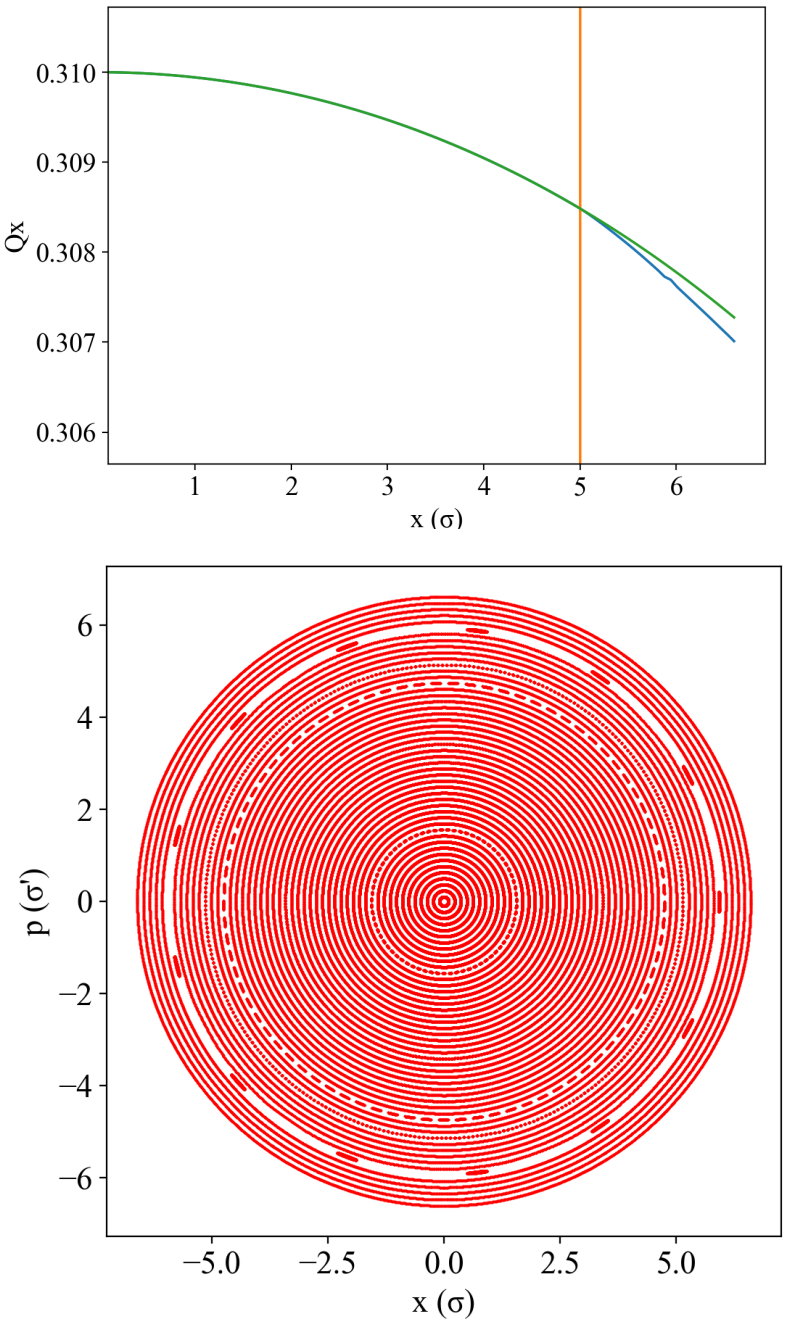

Figure 5.4: Preliminary study of a 2D HEL map, where only the mean of the noise is considered. In this simulation of 4096 iterations, the noise mean applied is 0.5 and $r_1 = 5\ \sigma_{\text{beam}}$. On top, tune Q_x as a function of the x coordinate. In yellow the coordinate of r_1, in green the unperturbed tune, in blue the actual tune perturbed by the noise mean. On the bottom, phase-space tracking of the map.

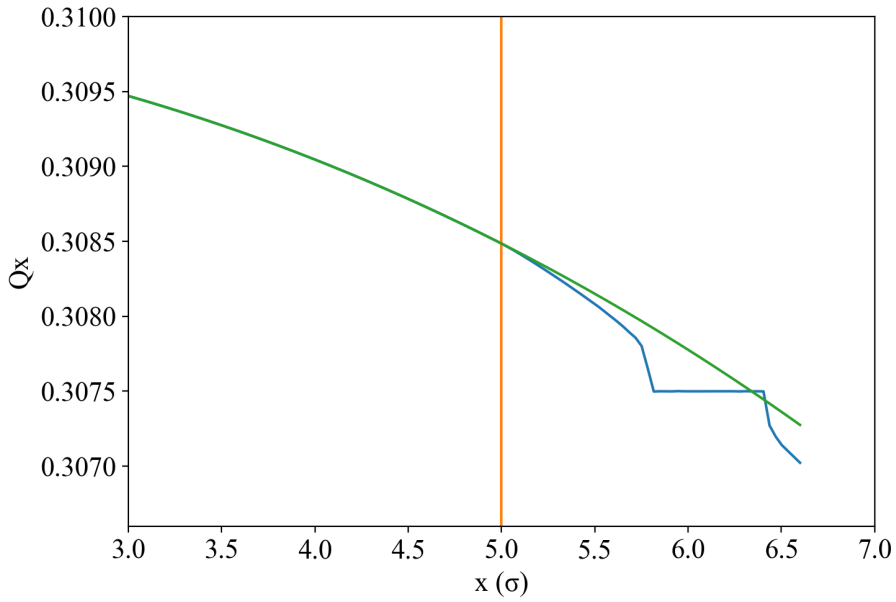

Figure 5.5: Preliminary study of a 2D HEL map, where a pure frequency $\omega/2\pi = 0.23$ was applied in order to induce resonance of order 4. In yellow the coordinate of $r_1 = 5\ \sigma_{\text{beam}}$, in green the unperturbed tune, in blue the actual tune with the modulation applied.

Chapter 6

Numerical Results

6.1 Map and Fokker-Planck comparison

In the following, we present the results for the 2D map simulations, and we compare them with the solutions of the Fokker-Planck equation. We performed the simulation of the map 4.11, where y and p_y were fixed at 0, so we only considered the dynamic in (x, p_x). The initial conditions of the beam are expressed in Section 5.1, where also the initial action distribution $\rho(I)$ is given. The simulation's parameters are given in Tab. 6.1 and the considered noise was $R_{0.5}[0, 1]$. We performed 10^6 iteration and observed the system evolution. The Fokker-Planck equation was

Table 6.1: Details of the parameters of the simulations. These have been used for every simulation performed, either in 2D or 4D case

Parameter	**Value**
Inner HEL radius, r_1 $[\sigma_{\text{beam}}]$	5
Outer HEL radius, r_2 $[\sigma_{\text{beam}}]$	10
Absorbing barrier, r_{a} $[\sigma_{\text{beam}}]$	6.7
n° of initial beam particles	10^6

integrated by means of a Crank-Nicolson integrator also used in [5], with a time step $\Delta\tau = 10^{-4}$, for up to 10^6 steps, and for a grid of 10^4 points in the action

interval $[r_1^2/2, r_a^2/2]$. Fig. 6.1 shows the comparison of action distribution between the map and the FP, at various steps of the simulation. We can see that the diffusive approach holds for the HEL case, and the FP equation is able to well approximate the time evolution of the action distribution.

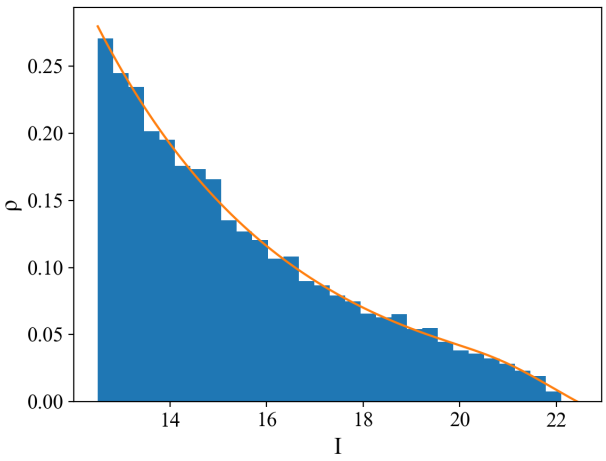

(a) $t = 10^3$

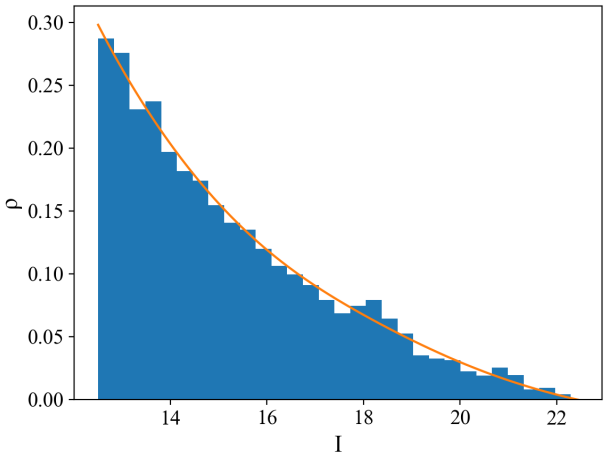

(b) $t = 10^4$

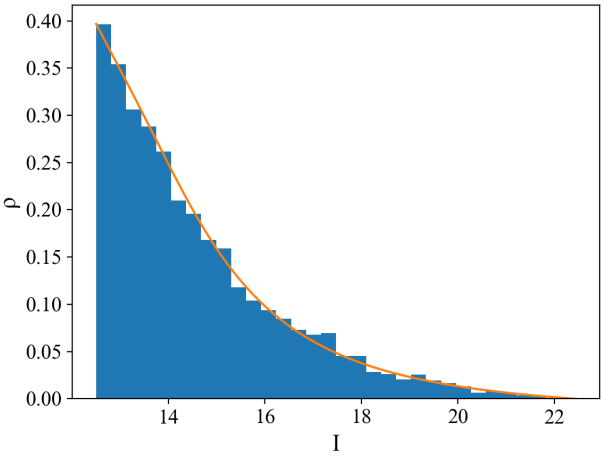

(c) $t = 10^5$

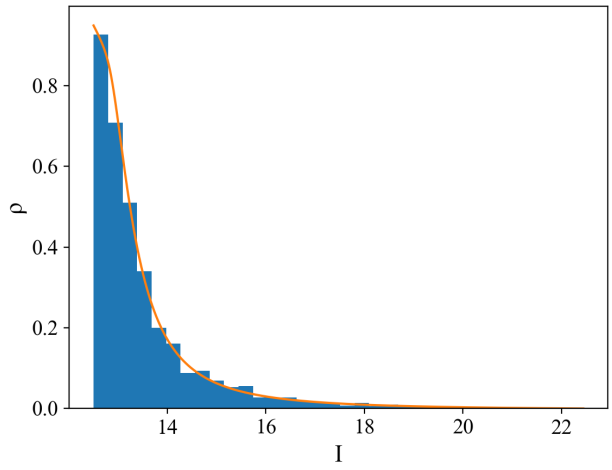

(d) $t = 10^6$

Figure 6.1: The figures show the comparison of the action distribution, between the map simulation, in blue, and the FP equation, in yellow, for different steps t of the simulation. Here the action is in units of $\sigma_{\text{beam}}^2/2$.

6.2 White noises comparisons

For this part of the study, we took into consideration various types of noise's distribution. We performed the simulation of the 2D map, as the previously discussed one, this time for $11 \cdot 10^5$ iterations, that could be interpreted as around 100 s of actual HL-LHC operation, knowing its frequency rotation is around $11 \cdot 10^3$ Hz. Here we were interested into the effects of different kinds of noises on the halo depletion efficiency. In Fig. 6.2, the simulations for the noise $R_{0.5}[0, 1]$ is displayed, while the simulation results for all the other noises are shown in the Appendix B. The results comparisons of the halo depletion, between the map simulations and the FP equation, are shown in Tab. 6.2. It is possible to see that, also here, there is agreement between the map and the FP results.

Table 6.2: Comparison between Crank-Nicolson and map simulation results, for various types of noise.

	Removed halo after 100 s [%]	
Noise	**Fokker-Planck**	**Map**
R_I	53.6	54.2
M_{12}	67.2	67.6
$R_{0.5}[0, 1]$	72.4	72.5
$R_{0.25}[0, 1]$	68.0	68.4
$R_{0.5}[0, 0.5]$	48.3	48.5
$R_{0.5}[0.75, 1]$	25.1	26.2

As expected, we observe differences in the halo cleaning performance among the various noise distributions. This is due to the different variances of the noises. Indeed, Eq. (4.27) gives the expression for the diffusion coefficient, and we have

$$D(I) \propto \sigma^2 \,, \tag{6.1}$$

where σ^2 is the variance of the noise. Thus, for higher variance noises, we observe a higher diffusion speed. To underline the link between diffusion speed and noise variance, we performed various map simulations with noises $R_p[a, b]$ of increasing

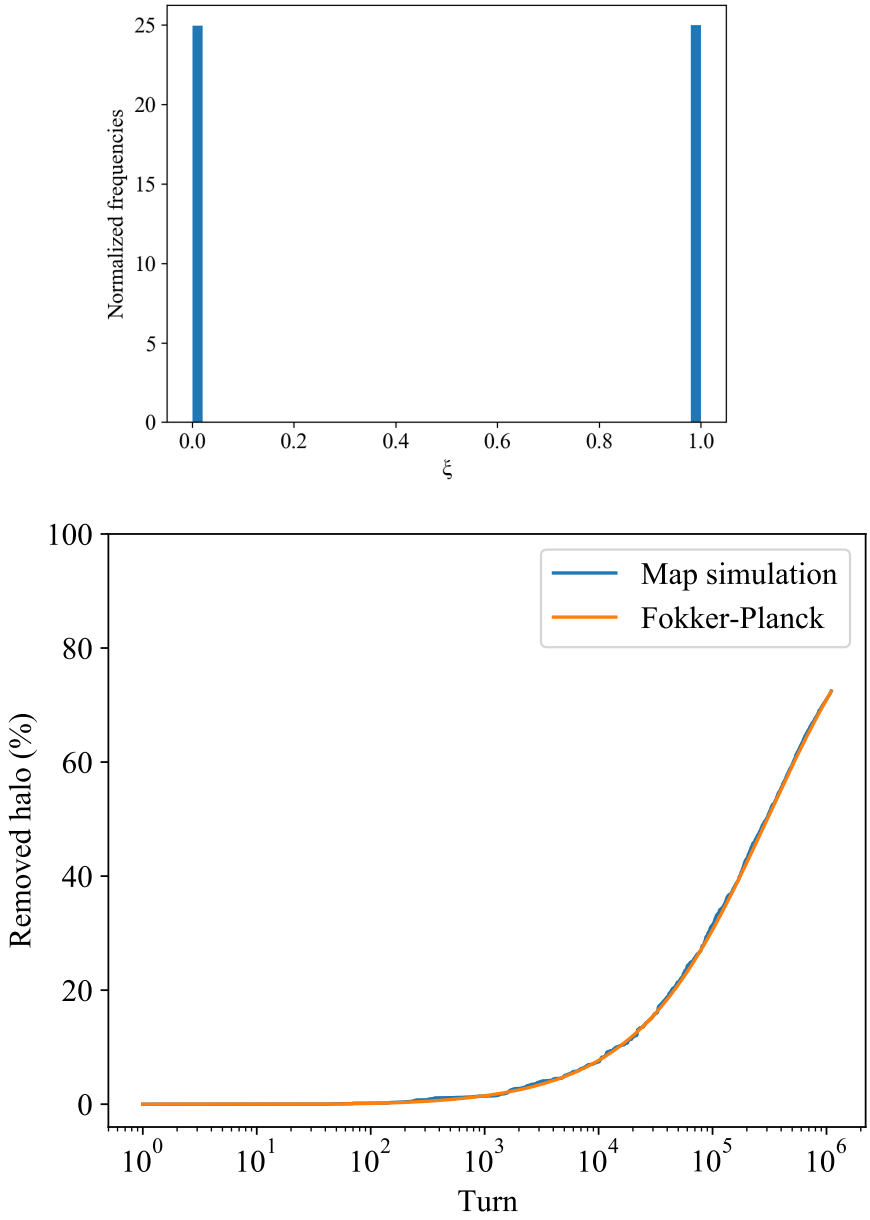

Figure 6.2: Top, noise distribution of $R_{0.5}[0, 1]$. Bottom, Removed halo as a function of machine turns, for the noise $R_{0.5}[0, 1]$, given by the map simulation (blue) and the FP (yellow). During the time evolution of the system, we observed a maximum absolute discrepancy between map simulation and FP of 1.3% of removed halo.

variance, by increasing the difference $b - a$ for every simulation. Moreover, to show that the discriminant between the diffusion speeds is not the noise distribution but rather its variance, we also plotted in the graph of Fig. 6.3 the results of the previous simulations, performed using the noises M_{12} and R_I.

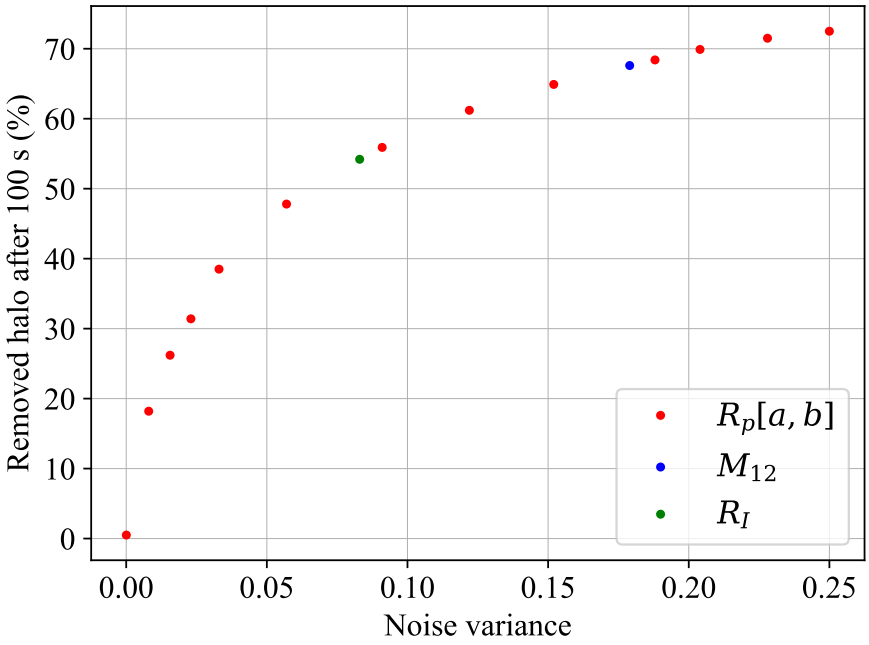

Figure 6.3: The image shows the results of the 2D map simulations for noises with different variances. As expected the variance of the noise plays the main role in the halo depletion speed, and even noises with different distributions follow the same trend.

6.3 Diffusion with correlated noises

In the last part of the thesis work, we searched for conditions that could allow to increase, as much as possible, the halo depletion, in order to have a faster and more efficient beam cleaning. All the parameters that characterised the previous simulations was kept fixed, and we acted only on the noise pattern. As shown in the previous section, we observed the diffusion effect of the white noise ceiling for

the noise having the largest variance, which in the interval [0,1] is 0.25. However, as discussed in Section 4.3, we expected to increase the diffusion by choosing a correlated noise, with the same variance, whose spectrum peaks at the frequency that satisfies the resonant condition (4.28). Thus we generated various correlated noises, using the algorithm discussed in Section 5.3, with frequency peaked within the frequency interval [0.11, 0.34]. For every noise we performed the 2D map simulation for around 100 s of actual HL-LHC operation. The results are shown in Fig. 6.4, where it is possible to observe the presence of two peaks of enhanced diffusion, with respect to the white noise ceiling of 72.5%, around frequencies 0.15 and 0.23. Indeed, these are the frequencies that, respectively, satisfy the resonant

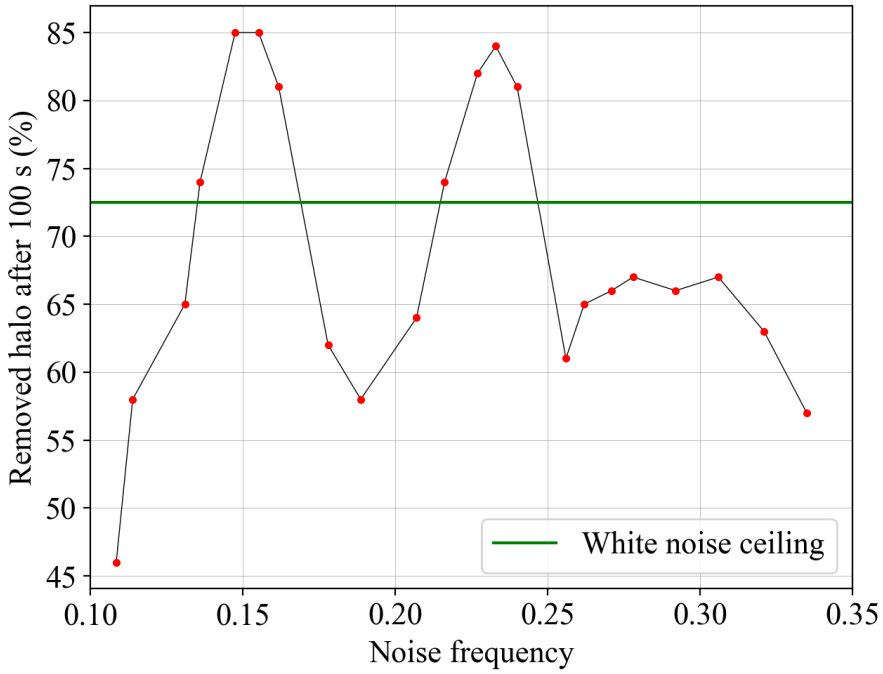

Figure 6.4: Results of 2D map simulations for different frequency peaked noises. The white noise ceiling of 72.5%, in green, is the removed halo after 100 s for the noise $R_{0.5}[0, 1]$. The two peaks that exceed the white noise ceiling are obtained using frequencies that induce resonances of order 4 and 6 in the system.

equations

$$6\Omega(I_{\mathrm{h}}) + \omega = 4\pi\,, \qquad 4\Omega(I_{\mathrm{h}}) - \omega = 2\pi\,, \tag{6.2}$$

that give the resonances of order 6 and 4. Here, I_{h} refers to the action in the halo region. Thus, for resonance-inducing noises, we observed a relative increase of up to 17% of the halo removal after 100 s, with respect to the white noise ceiling. While the odd resonances were absent in the system, the resonance of order 2 was, indeed, present; however, the frequency to induce that would be around 0.38, which was outside the interval of the noise generation.

To prove that this phenomenon is not a peculiarity of the 2D simplified model, this time we also iterated the same kind of simulations for the 4D map, considering always the same simulation's parameter values used up to this moment. We performed these simulations for 387822 iterations which correspond to around 35 s of real time operation. The results are displayed in Fig. 6.5.

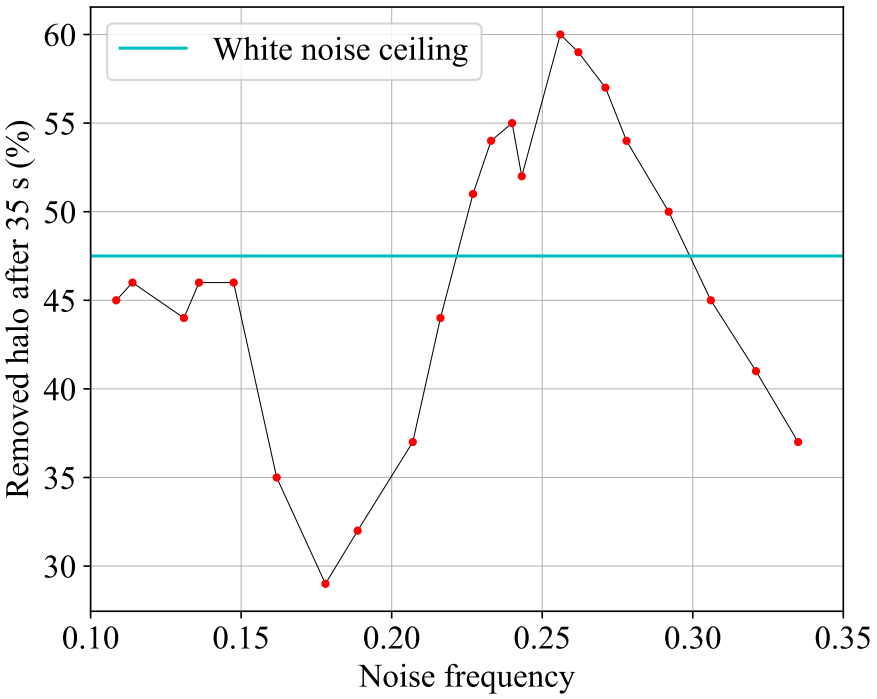

Figure 6.5: Results of 4D map simulations for different frequency peaked noises. The white noise ceiling of 47.5%, in cyan, is the removed halo for the noise $R_{0.5}[0, 1]$ after 35 s. As one can see, the peaks of diffusion are present also in the 4D case.

Also in the 4D case, we observed an enhance of the diffusion for certain values of the frequency peak of the noise, and a relative increase of up to 26% of the halo

removal after 35 s, with respect to the white noise ceiling. This time, the locations of the peaks are different due to the addition of the dynamic in (y, p_y), which possesses a different tune. Making further tests, varying the machine nominal tunes, we observed that the big peak in Fig. 6.5 is possibly the result of the superposition of multiple peaks. Indeed the added layer of complexity of the 4D case made harder to recognise the identity of the resonances; however, here we were only interested into showing that the possibility to enhance the diffusion with correlated noises was not a peculiarity of the 2D case.

Chapter 7

Conclusions

In this master thesis, we showed the possibility to describe the behaviour of the beam-halo depletion, under the effect of a simplified HEL system, using a diffusive framework. We showed that the evolution of the action distribution of the beam $\rho(I)$ is well approximated by a Fokker-Planck equation. We focused on the study of various types of white noise distribution and we observed their effects on the diffusion speed of the halo.

All the results were well predicted by the the diffusion model, in particular the role of the variance of noise distribution in the phenomenon. Moreover we explored the possibility to exceed the maximum diffusion speed, guaranteed by the white noise, by inducing resonances in the system with correlated noises. Indeed, we found a way to generate a peculiar colored noise that allowed us to obtain a non-negligible increment of up to 17% of removed halo after 100 s, with respect to the white noise case.

7.1 Future developments

Further developments will aim to bring this approach to more complex and realistic models of the HEL system, namely the 6D scenarios, in which all the dynamics and elements of HL-LHC are considered. A more consistent and quantitative study on the effects of correlated noises in the HEL diffusion has to be performed in the

future. In particular, the explicit computation of the diffusion coefficient $D(I)$, for this scenario, is necessary to make numerical comparisons between the model and the simulations. Furthermore, the opportunity to perform deeper and more realistic beam simulations for the HEL, with the ad hoc noise we have created to enhance the halo depletion, should be pursued, in light of the possibility to apply it to the real case of the HL-LHC.

Appendix A

HEL kick derivation

Let us consider an infinitely long beam of relativistic electrons travelling with speed $\vec{v}_e$ antiparallel to axis $\hat{s}$. Having a cylindrical symmetry with respect to $\hat{s}$ axis, all the longitudinal components of the electromagnetic field compensate each other and only the radial ones survive. Thus, the equations for electric and magnetic fields in the laboratory frame are [24]

$$\begin{cases} E_{lab} = \gamma_e E_r \\ B_{lab} = \gamma_e \frac{v_e}{c^2} E_r \end{cases}, \tag{A.1}$$

where E_r is the radial component of the electric field. If we now consider a proton traveling with speed $\vec{v}$ in the direction $\hat{s}$ (thus opposite to the electrons), it will experience a Lorentz force directed radially given by

$$F_r = q[\vec{E}_{lab} + v\vec{B}_{lab}] = q\gamma_e[1 + \beta_e\beta_p]E_r, \tag{A.2}$$

where q is the charge of the proton, β_p and β_e are the relativistic factors of the proton and electron beams, respectively. If the proton travels in the same direction as the electron, a $-$ sign appears instead of the $+$, thus we write

$$F_r = q\gamma_e[1 \mp \beta_e\beta_p]E_r. \tag{A.3}$$

It is possible to express the variation of transverse momenta of the proton imparted by the electron beam as

$$\Delta p_z = \frac{\int_{t_1}^{t_2} F_z(t)dt}{p} \tag{A.4}$$

where z stands for x or y, F_z is the Lorentz force, and p is the proton momentum. Assuming that the proton travels parallel to the electron and that F_z is constant along the lens, we have the following.

$$\Delta p_z = \frac{F_z(s)}{vp} \int_{s_1}^{s_2} ds = \frac{F_z L}{vp} \tag{A.5}$$

where we moved to longitudinal coordinates by the relation $t = s/v$. Expressing the electric field along z as

$$E_z = E_r \frac{z}{r} \tag{A.6}$$

we rewrite the kick as

$$\Delta p_z = \frac{q}{p} \gamma_e [1 \mp \beta_p \beta_e] \frac{L}{\beta_p c} E_r(r) \frac{z}{r} \,. \tag{A.7}$$

The flux of the electric field generated by the electron beam is

$$\phi(\vec{E}) = 2\pi r L E_r(r), \tag{A.8}$$

while the charge inside the cylindrical surface of radius r is

$$Q = I \Delta t f(r) = I \frac{L}{\beta_e c} f(r), \tag{A.9}$$

where I is the total current of the electrons, Δt is the flight time through the lens, and $f(r)$ is the geometrical function depending on the electron distribution. Taking into account a hollow electron beam, $f(r)$ is given by

$$f(r) = \begin{cases} 0 & r \leq R_1 \\ \tilde{f}(r) = 2\pi \int_{R_1}^{r} \rho(r') r' dr' & R_1 < r < R_2 \\ 1 & r \geq R_2 \end{cases} , \tag{A.10}$$

where R_1 and R_2 are the inner and outer radius of the lens respectively, and $\rho(r')$ is the radial charge distribution of the electrons. Applying the Gauss theorem and solving for E_r we find

$$E_r = \begin{cases} 0 & r \leq R_1 \\ \frac{I}{2\pi\epsilon_0 \beta_e c} \frac{\tilde{f}(r)}{r} & R_1 < r < R_2 \\ \frac{I}{2\pi\epsilon_0 \beta_e c} \frac{1}{r} & r \geq R_2 \end{cases} , \tag{A.11}$$

which replaced in Eq. (A.7) gives

$$\Delta p_z = \frac{qLI}{2\pi\epsilon_0 c^2 p}\gamma_e \frac{1 \mp \beta_p\beta_e}{\beta_p\beta_e}\frac{f(r)}{r}\frac{z}{r} = \hat{\theta}_{\max}\frac{f(r)}{r/R_2}\frac{z}{r}, \tag{A.12}$$

where

$$\hat{\theta}_{\max} = \frac{LI\gamma_e(1 \mp \beta_p\beta_e)}{2\pi\epsilon_0 c^2 (B\rho)_p \beta_p\beta_e R_2}, \tag{A.13}$$

where we used the definition of magnetic rigidity $B\rho = p/q$.

The function $f(r)$ is normalised if

$$2\pi\int_{R_1}^{R_2}\rho(r')r'dr' = 1, \tag{A.14}$$

and for a constant radial profile we have that

$$\rho(r) = A, \tag{A.15}$$

where A is the normalisation constant. Then solving Eq. (A.14) for A we get

$$A = \frac{1}{2\pi\int_{R_1}^{R_2} r'dr'} = \frac{1}{\pi[R_2^2 - R_1^2]} = \rho(r). \tag{A.16}$$

The cumulative distribution $\tilde{f}(r)$ can be rewritten as

$$\tilde{f}(r) = \frac{2\pi\int_{R_1}^{r} r'dr'}{\pi[R_2^2 - R_1^2]} = \frac{r^2 - R_2^2}{R_2^2 - R_1^2}, \tag{A.17}$$

and the final form of $f(r)$ is

$$f(r) = \begin{cases} 0 & r \le R_1 \\ \frac{r^2 - R_2^2}{R_2^2 - R_1^2} & R_1 < r < R_2 \\ 1 & r \ge R_2 \end{cases}. \tag{A.18}$$

Appendix B

Supplementary simulations results

In the following, we present the graphs referring to the results discussed in Section 6.2.

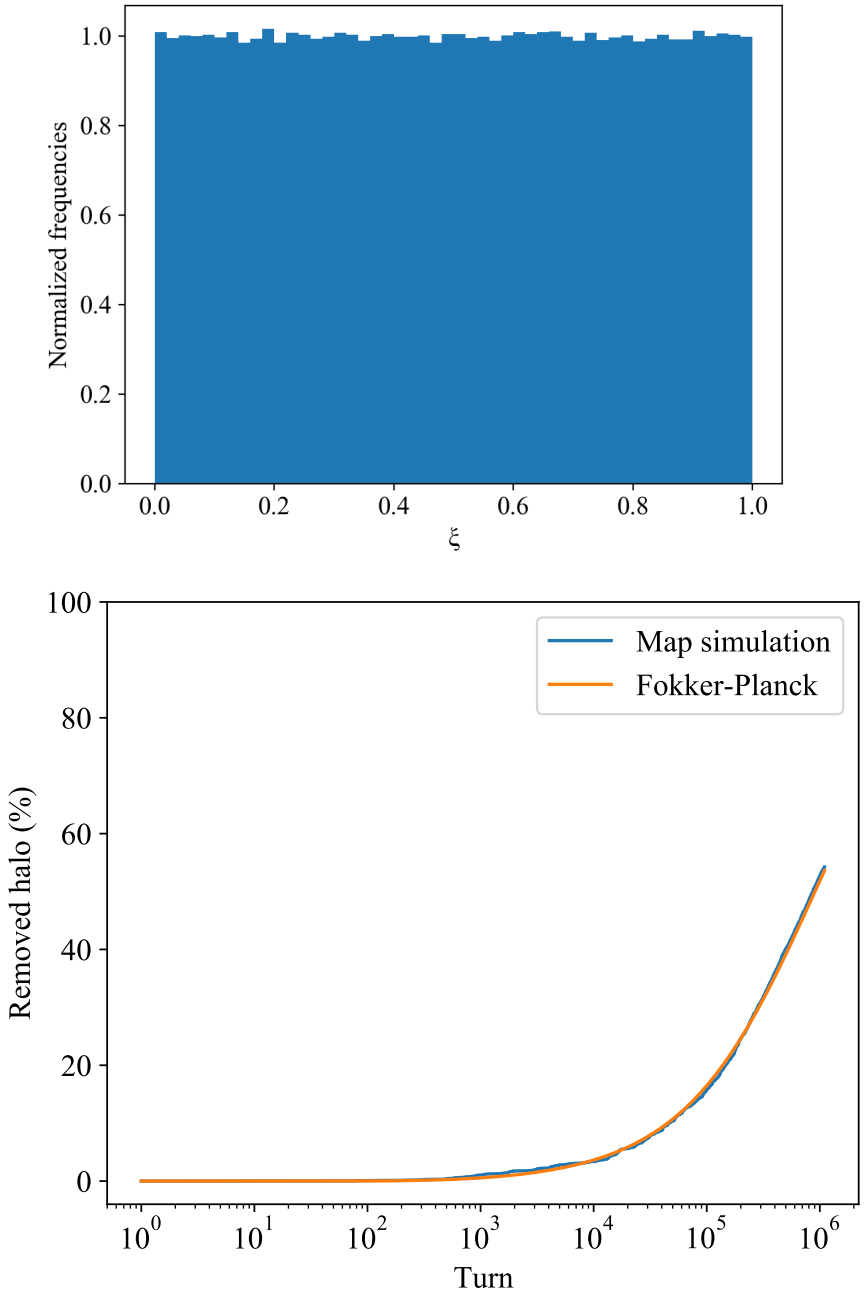

Figure B.1: Top, noise distribution of R_I. Bottom, Removed halo as a function of machine turns, for the noise R_I, given by the map simulation (blue) and the FP (yellow).

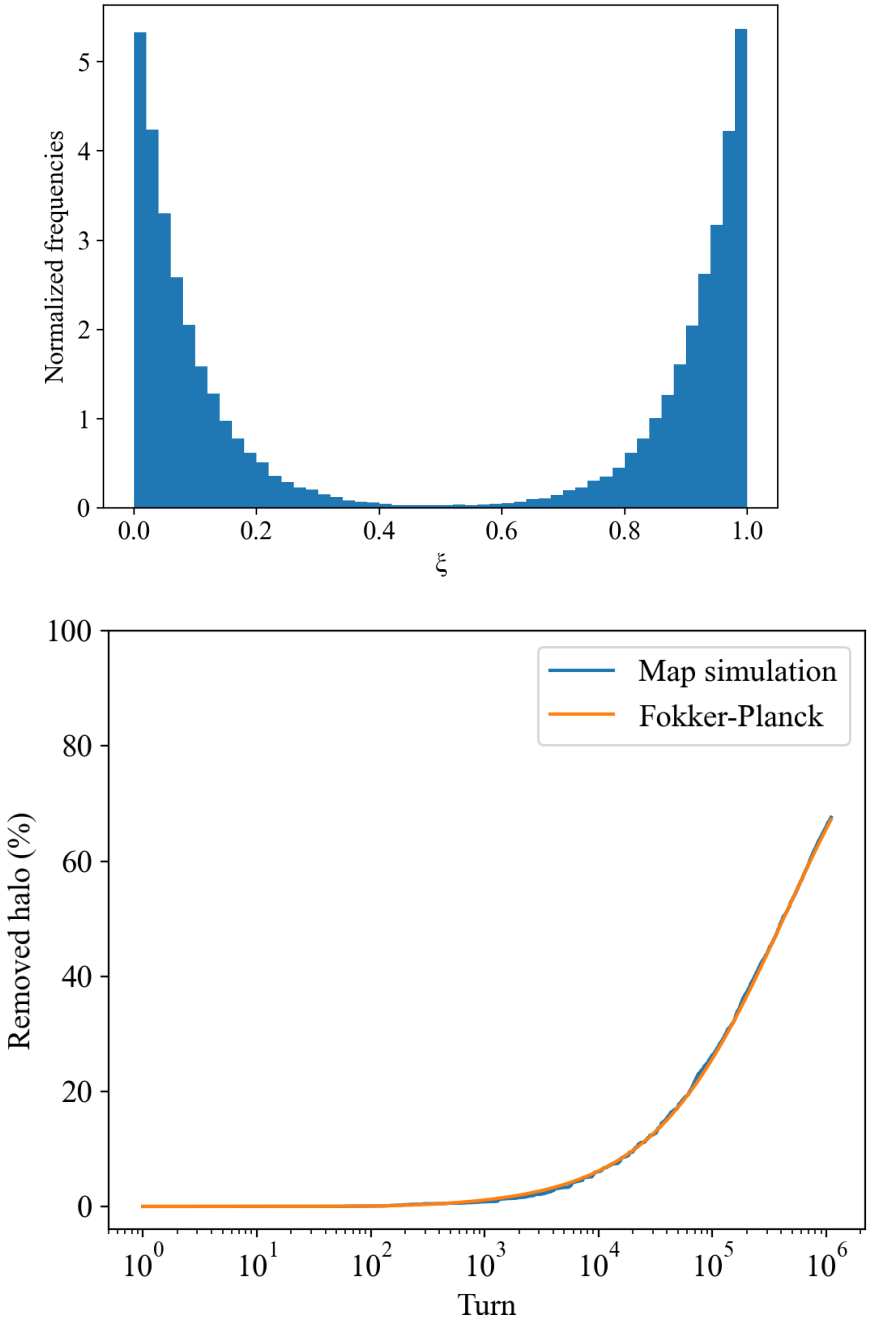

Figure B.2: Top, noise distribution of M_{12}. Bottom, Removed halo as a function of machine turns, for the noise M_{12}, given by the map simulation (blue) and the FP (yellow).

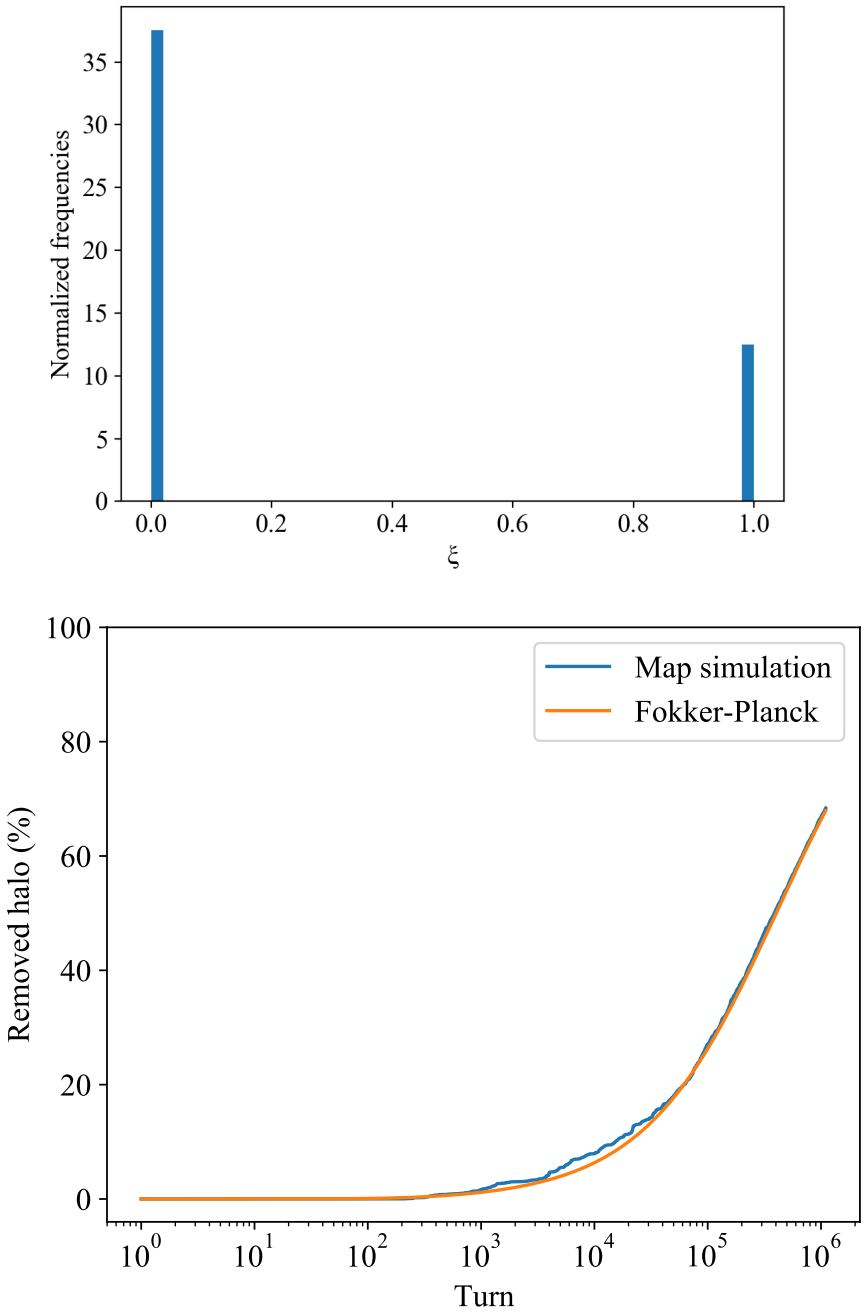

Figure B.3: Top, noise distribution of $R_{0.25}[0,1]$. Bottom, Removed halo as a function of machine turns, for the noise $R_{0.25}[0,1]$, given by the map simulation (blue) and the FP (yellow).

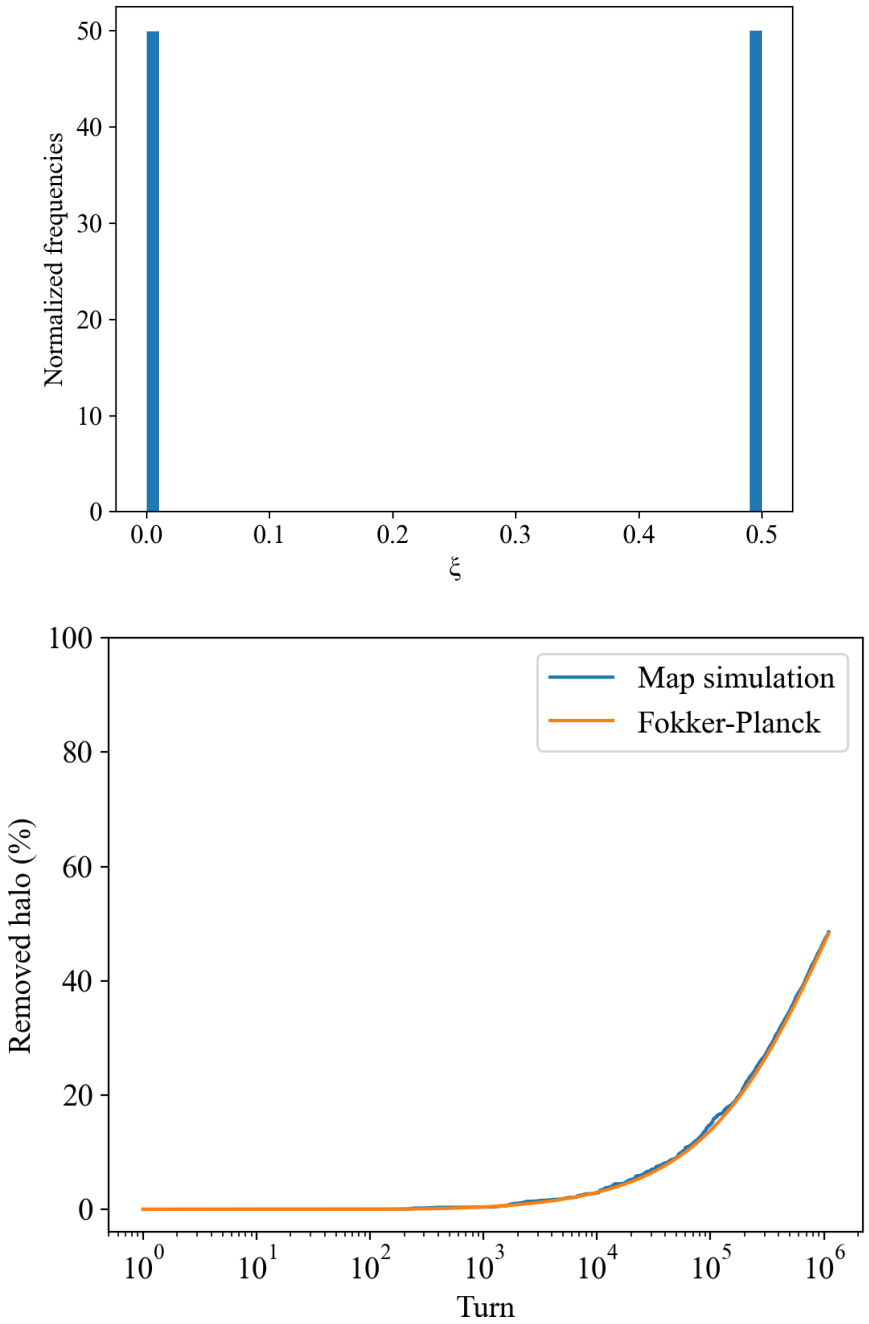

Figure B.4: Top, noise distribution of $R_{0.5}[0, 0.5]$. Bottom, Removed halo as a function of machine turns, for the noise $R_{0.5}[0, 0.5]$, given by the map simulation (blue) and the FP (yellow).

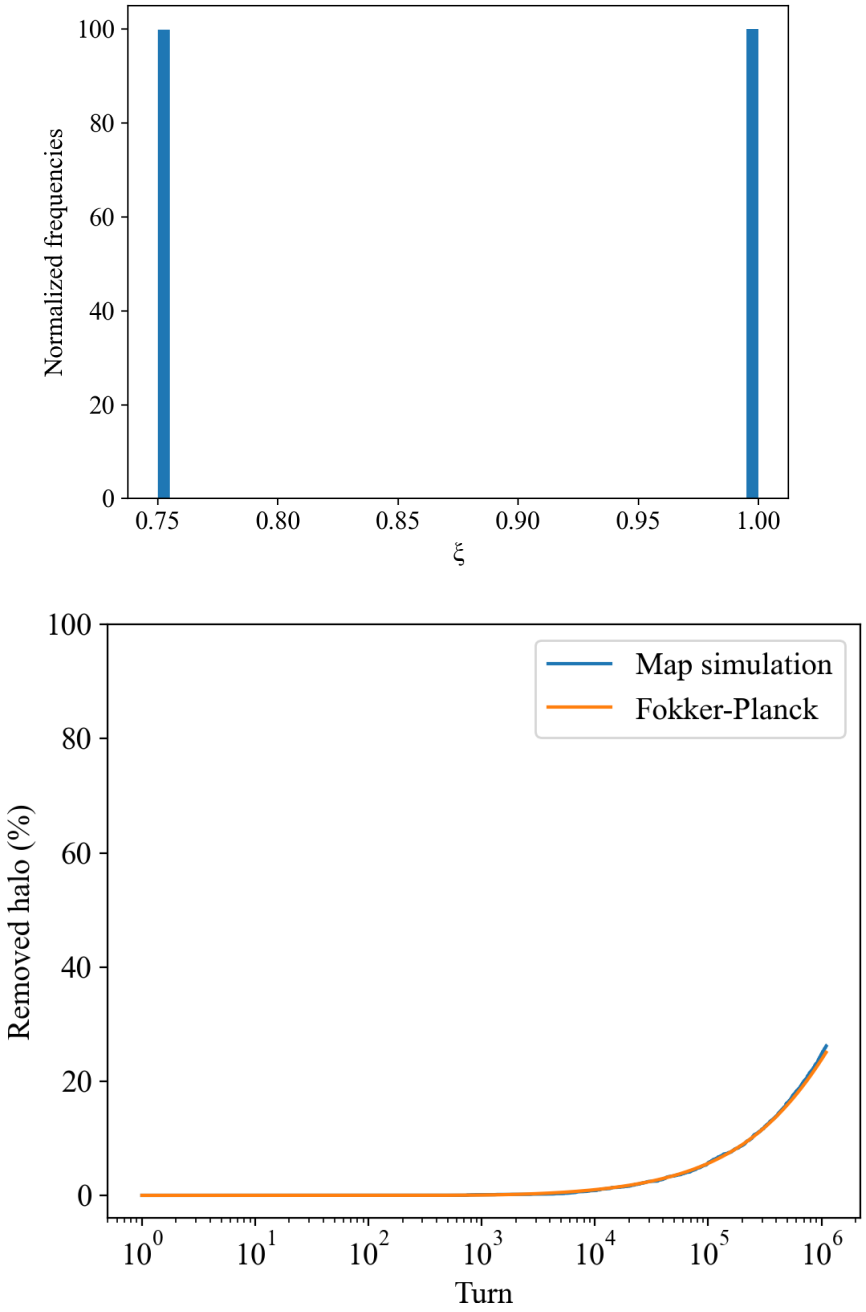

Figure B.5: Top, noise distribution of $R_{0.5}[0.75, 1]$. Bottom, Removed halo as a function of machine turns, for the noise $R_{0.5}[0.75, 1]$, given by the map simulation (blue) and the FP (yellow).

Bibliography

[1] I. Béjar Alonso, O. Brüning, P. Fessia, L. Rossi, L. Tavian and M. Zerlauth, **High-Luminosity Large Hadron Collider (HL-LHC): Technical design report.**, CERN Yellow Reports: Monographs CERN, Geneva (2020).

[2] G. Stancari, A. Valishev, G. Annala, G. Kuznetsov, V. Shiltsev, D. A. Still et al, **Collimation with hollow electron beams**, Phys. Rev. Lett. 107 (2011).

[3] S. Redaelli et al., **Hollow electron lenses for beam collimation at the High-Luminosity Large Hadron Collider (HL-LHC)**, Journal of Instrumentation 16 (2021).

[4] D. Mirarchi, et al., **Nonlinear dynamics of proton beams with hollow electron lens in the CERN high-luminosity LHC**, Eur. Phys. J. Plus 137 (2022).

[5] C.E. Montanari **Diffusive approach for non-linear beam dynamics in a circular accelerator**, Master thesis Bologna University, CERN-THESIS-2019-383, (2019).

[6] Z. Li, Z. Qiao and T. Tang, **Numerical Solution of Differential Equations: Introduction to Finite Difference and Finite Element Methods**, Cambridge University Press, DOI: 10.1017/9781316678725, Cambridge (2017).

[7] S. Lee, **Accelerator Physics**, *2nd ed.* World Scientific, URL: `https://cds.cern.ch/record/939203`, London (2004).

[8] A. Bazzani, E. Todesco, G. Servizi and G. Turchetti **A normal form approach to the theory of nonlinear betatronic motion**, CERN 94-02 (CERN, 1994).

[9] E.H. Maclean **Modelling and correction of the non-linear transverse dynamics of the LHC from beam-based measurements**, Ph.D. thesis, University of Oxford (Trinity 2014).

[10] E. Courant and H. Snyder, Ann. Phys. 3, 1 (1958).

[11] E. Todesco and M. Giovannozzi **Dynamic aperture estimates and phase-space distortions in nonlinear betatron motion**, Phys. Rev. E 53 (1996).

[12] J.J. Shynk, **Probability, Random Variables, and Random Processes: Theory and Signal Processing Applications** (2012)

[13] I. Karatzas, S.Shreve, **Brownian Motion and Stochastic Calculus** (1991)

[14] A. Bazzani, and M. Giovannozzi, and E.H. Maclean, **Analysis of the non-linear beam dynamics at top energy for the CERN Large Hadron Collider by means of a diffusion model**, Eur. Phys. J. Plus 135, DOI: 10.1140/epjp/s13360-020-00123-2 (2019).

[15] A. Bazzani, L. Beccaceci, L. Bigliardi, G. Turchetti, **Fokker-Planck solutions for action diffusion in a noisy symplectic map**, AIP Conf. Proc. 395, 109 (1997).

[16] A. Bazzani, and S. Siboni, and G. Turchetti, **Diffusion in Hamiltonian systems with a small stochastic perturbation**, Physica D Nonlinear Phenomena 76 (1994).

[17] D. Mirarchi, G. Arduini, M. Giovannozzi, A. Lechner, S. Redaelli, and J. Wenninger, **Special Losses during LHC Run 2**, in 9th LHC Operations Evian Workshop, Geneva (2019).

[18] A. Gorzawski, R. Appleby, M. Giovannozzi, A. Mereghetti, D. Mirarchi, S. Redaelli et al., **Probing LHC halo dynamics using collimator loss rates at 6.5 tev**, Physical Review Accelerators and Beams 23, (2020).

[19] B. Lindstrom et al., **Fast failures in the LHC and the future high luminosity LHC**, Phys. Rev. Accel. Beams 23 (2020).

[20] X. Gu et al., **Halo removal experiments with hollow electron lens in the BNL Relativistic Heavy Ion Collider**, Phys. Rev. Accel. Beams 23 (2020).

[21] `http://sixtrack.web.cern.ch/SixTrack/`.

[22] M. Fitterer, G. Stancari, A. Valishev, **Resonant and random excitations on the proton beam in the Large Hadron Collider for active halo control with pulsed hollow electron lenses**, Phys. Rev. Accel. Beams **24** 021001 (2021).

[23] P. Hermes, private communication (2021).

[24] M. Giovannozzi, private communication (2022).

[25] A. Bazzani and L. Beccaceci, **Diffusion in Hamiltonian systems driven by harmonic noise**, J. Phys. A - Math. Gen. **31**, 5843 (1998).

[26] M. Mestre, A. Bazzani, P. Cincotta, and C. Giordano, **Stochastic approach to diffusion inside the chaotic layer of a resonance**, Phys. Rev. E **89**, 012911 (2014)